RMetS
Royal Meteorological Society

Clear-sky stable boundary layers with low winds over snow-covered surfaces. Part 1: WRF model evaluation

H. A. M. Sterk,[a]* G. J. Steeneveld,[a] T. Vihma,[b] P. S. Anderson,[c] F. C. Bosveld[d] and A. A. M. Holtslag[a]

[a]*Meteorology and Air Quality Section, Wageningen University, the Netherlands*
[b]*Finnish Meteorological Institute, Helsinki, Finland*
[c]*Scottish Association for Marine Science, Oban, UK*
[d]*Royal Netherlands Meteorological Institute, De Bilt, the Netherlands*

*Correspondence to: H. A. M. Sterk, Meteorology and Air Quality Section, Wageningen University, PO Box 47, 6700 AA Wageningen, the Netherlands. E-mail: Marina.Sterk@wur.nl

In this article, we evaluate the Weather Research and Forecasting (WRF) mesoscale meteorological model for stable conditions in clear skies with low wind speeds. Three contrasting terrains with snow-covered surfaces are considered, namely Cabauw (Netherlands, snow over grass), Sodankylä (Finland, snow over a needle-leaf forest) and Halley (Antarctica, snow over an ice shelf). We used the full three-dimensional (3D) model and the single-column versions of the WRF model. The single-column model (SCM) was driven by realistic forcings of the WRF–3D field. Several sets of SCM forcings were tested: A, no advection; B, varying geostrophic wind in time; C, momentum advection in addition to B; D, temperature and moisture advection in addition to C; E, forcing the SCM field to the 3D field above a threshold height.

The WRF–3D model produced good results overall for wind speed, but the near-surface temperatures and specific humidity were overestimated for Cabauw and Sodankylä and underestimated for Halley. Prescribing advection for momentum, temperature and moisture gave the best results for the WRF–SCM and simulations deviated strongly from reality without advection. Nudging the SCM field to the 3D field above a threshold height led to an unrealistic behaviour of the variables below this height and is not recommended. Detailed prescription of the surface characteristics, e.g. adjusting the snow cover and vegetation fraction, improved the 2 m temperature simulation. For all three sites, the simulated temperature and moisture inversion were underestimated, though this improved when prescribing advection.

Overall, in clear-sky conditions, the stable boundary layer over snow and ice can be modelled to a good approximation if all processes are taken into account at high resolution and if land surface properties are carefully prescribed.

Key Words: stable boundary layer; single-column model; WRF; model evaluation; snow surface; low wind speeds

Received 20 February 2014; Revised 15 December 2014; Accepted 23 December 2014; Published online in Wiley Online Library

1. Introduction

The evolution of the stable boundary layer (SBL) is mostly determined by turbulent mixing, the coupling between the atmosphere and the surface and radiative effects. Additionally, the presence of clouds or fog, subsidence, geostrophic wind speed, advection, gravity waves and drainage and katabatic flows may play a role (Delage, 1997; Mahrt *et al.*, 1998; Mahrt, 1999; Steeneveld *et al.*, 2006; Williams *et al.*, 2013). The reason why SBL modelling remains complex could be related to the large amount of relatively small-scale processes that may act simultaneously and interactively, while on top of that the physical processes and their interactions are also not completely understood and are represented incompletely in models.

Furthermore, a large variety of SBL types exists, e.g. there can be continuous or intermittent turbulence or even laminar flow, which influences the SBL depth and the vertical and horizontal exchange of quantities (e.g. Holtslag *et al.*, 2013). A relatively coarse resolution (e.g. in operational models) can also hamper proper SBL modelling (e.g. Steeneveld *et al.*, 2006; Tardif, 2007; Byrkjedal *et al.*, 2008; Svensson and Holtslag, 2009; Svensson and Karlsson, 2011; Savijärvi, 2013). Especially over snow-covered polar surfaces, where atmospheric conditions can become very stable, modelling the SBL is challenging. For example, in the

Arctic and Antarctic, many global and regional climate model outputs diverge from one another, as well as from observations (e.g. Holland and Bitz, 2003; Rinke *et al.*, 2006; Walsh *et al.*, 2008; Rinke *et al.*, 2012; Valkonen *et al.*, 2013). Though simplified model representation of SBL processes may not be the only cause of these model biases, we will focus on the SBL processes in this article.

Single-column models (SCMs) are convenient to evaluate the physical processes in the boundary layer (BL) and can therefore be used to improve our understanding of SBL processes (Baas *et al.*, 2010; Sterk *et al.*, 2013; Bosveld *et al.*, 2014b). Therefore, in this study the SCM version of the Weather Research and Forecasting (WRF: Skamarock *et al.*, 2008) mesoscale meteorological model is evaluated for stable conditions over snow-covered surfaces. To evaluate the model performance against observations, the SCM needs to be driven by realistic forcings of the 3D atmospheric field (Baas *et al.*, 2010; Bosveld *et al.*, 2014a). A complete observational dataset at high temporal resolution is typically not always available, due e.g. to low temporal data coverage, possible equipment failure with low temperatures and measurement stations that are limited spatially or do not measure all required quantities. Therefore we rely on 3D model results to determine the SCM large-scale forcings, which is also advantageous, since some aspects of the forcings are difficult to measure. We perform WRF–3D runs to determine the SCM forcings and evaluate the WRF–3D runs briefly.

In Part 1 of this study, we evaluate the model for stable conditions with approximately the same low wind speeds for three contrasting terrains with snow, i.e. from the Cabauw site in the Netherlands, the Sodankylä site in northern Finland and the Halley station on Antarctica. These sites are characterized by snow over grass/cropland, snow in an evergreen needle-leaf forest and snow on an ice sheet, respectively. For all terrain types, a case is selected with little to no cloud cover, as then stable stratifications are more likely to develop, while additionally this reduces the complexity of the radiative transfer. This makes the interpretation when studying the interaction of the snow surface and the SBL less difficult. Furthermore, because models often have problems simulating stable cases with relatively low wind speeds (Edwards *et al.*, 2011; Tastula and Vihma, 2011; Holtslag *et al.*, 2013), the selected study periods have low wind speeds as well. Such SBLs are typically referred to as so-called type I SBLs, for which, with very stable temperature stratifications and low wind speeds, radiative cooling is the dominating process and the vertical potential temperature (θ) profile is more exponentially (or concave up, $\partial^2\theta/\partial z^2 < 0$) shaped (Van Ulden and Holtslag, 1985; Vogelezang and Holtslag, 1996). Van de Wiel *et al.* (2012) report on a minimum wind speed under clear-sky conditions below which sustainable, continuous turbulence is unlikely and a very stable boundary layer is more likely. At the so-called crossing level of 40 m at Cabauw (the height where wind is relatively stationary compared with other levels), this minimum wind speed is $\sim$5–7 m s^{-1}.

Apart from the WRF–SCM model evaluation for SBLs over snow for various land use types under low wind regimes, we will discuss how to determine the required forcings for running the SCM. We compare runs where only initial profiles are given, as well as ones where advection is prescribed, and report on experiences with a straightforward nudging approach above the BL.

SCMs are also a convenient tool for sensitivity analyses, because parameters can be controlled without introducing strong 3D effects. Focusing on the Arctic, Sterk *et al.* (2013) performed a sensitivity analysis of the snow-surface coupling, radiation and turbulent mixing, since these mostly control the SBL evolution and structure (André and Mahrt, 1982; Beljaars and Holtslag, 1991; Steeneveld *et al.*, 2006; Bosveld *et al.*, 2014b). Due to their idealized set-up, a direct comparison with observations was not possible. Therefore we extend their sensitivity analysis in Part 2 of this study, using the real-world cases defined in the current article as a reference. In this way, we study how the importance of the processes shifts and whether the model sensitivity varies between certain processes over different terrains. As such, we hope to gain more insight into where future research efforts should be focused.

This article is organized as follows. In section 2, an overview of the case studies and observational data is presented, together with their accompanying synoptic settings. Section 3 gives an explanation of the WRF model, after which the methodology is described in section 4. This is followed by the results in section 5 and conclusions and discussions in section 6.

2. Observational data

The three locations and selected cases are described below. The first criterion for the case selection was that no clouds were observed. We checked this from either the observed cloud fraction and/or the downwelling long-wave radiation. The second criterion was that the tower observations indicated strongly stable conditions. Furthermore, near-surface wind speeds had to be relatively low (less than 5 m s^{-1}), while soundings indicated relatively low wind speeds up to at least 1.5 km as well. Table 1 summarizes the characteristics during the SCM study periods.

2.1. Cabauw

The first dataset that we will study has been obtained from the Cabauw Experimental Site for Atmospheric Research (Cesar) observatory, located in a flat area in the western part of the Netherlands (51.97°N, 4.93°E). At this site, profiles of wind speed and wind direction from the Cabauw tower at 10, 20, 40, 80, 140 and 200 m height were available. At these heights and at the 2 m level, temperature and relative humidity were also

Table 1. Characteristics of the Cabauw, Sodankylä and Halley sites during the SCM study periods, from both observations and settings in the WRF–SCM simulations. Observed quantities are as follows: latitude and longitude (lat/lon), land use, snow depth (not at Halley), near-surface wind speed ($U_{\mathrm{tot\,near-sfc}}$), wind speed at the top of the mast ($U_{\mathrm{tot\,top-mast}}$), minimum 2 m temperature ($T_{\mathrm{2m\,min}}$) and observed temperature gradient along the mast at the end of the SCM study period (ΔT_{mast}). Model-based characteristics are as follows: roughness length applied in the WRF–SCM (z_0, from observations at Halley) and geostrophic wind speeds applied for the WRF–SCM ($U_{\mathrm{geo\,3D-WRF}}$, from WRF–3D).

	Cabauw	**Sodankylä**	**Halley**
Lat/lon	51.97°N, 4.93°E	67.36°N, 26.63°E	75.58°S, 26.65°W
Land use	Grass	Forest, bogs, shrubland	Ice shelf
Snow depth	3.5 cm	62 cm	Gradual transition to ice in reality 6.2 cm in WRF–3D
$U_{\mathrm{tot\,near-sfc}}$	0.7–3.5 m s^{-1} (at 10 m)	0–1.5 m s^{-1} (at 10 m)	2.5–4.7 m s^{-1} (at 8 m)
$U_{\mathrm{tot\,top-mast}}$	2.6–7.6 m s^{-1} (at 200 m)	0–2.7 m s^{-1} (at 47 m)	2.1–4.7 m s^{-1} (at 32 m)
$T_{\mathrm{2m\,min}}$	253.4 K	244 K	240.5 K
ΔT_{mast}	11.6 K (2–200 m)	9 K (3–48 m)	14 K (1–32 m)
z_0	1 mm	0.5 m	0.056 mm
$U_{\mathrm{geo\,3D-WRF}}$	2.6–5.9 m s^{-1} (2.3–6 m s^{-1} observed)	0.4–2.6 m s^{-1}	3.5–7.3 m s^{-1}

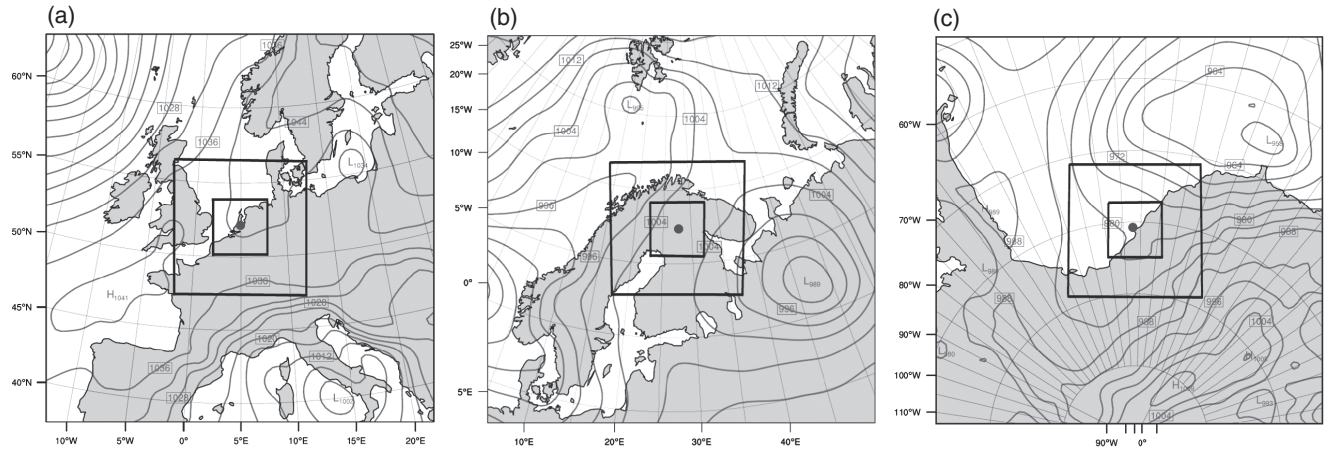

Figure 1. Mean sea-level pressure in contours (hPa) for (a) the Cabauw case, 4 February 2012, 0000 UTC, (b) the Sodankylä case, 27 March 2009, 0000 UTC, and (c) the Halley case, 18 May 2003, 1200 UTC. The study sites are indicated by dots. The outer and inner domain for the WRF–3D runs are indicated by squares.

measured. Furthermore, all components of the surface radiation and energy budget were available from this measurement site. Further details on the measurement site and information on the different instruments used are found in Van Ulden and Wieringa (1996), Beljaars and Bosveld (1997) and CESAR (2013).

The cloud-free night of 3–4 February 2012 was selected, since very low temperatures were reached over the fresh snow cover that had fallen in the morning and afternoon of 3 February. The prevailing weather was determined by a blocking high-pressure system located over Scandinavia and northwest Russia reaching to the British Isles (KNMI, 2012, see Figure 1(a)). This indicated winds coming from the east to north. Wind speeds at 10 m ($U_{\mathrm{tot\,10m}}$) were about 0.7–3.5 m s^{-1}; at 200 m this varied between 2.6 and 7.6 m s^{-1}. The surface geostrophic wind speed obtained from analyzing surface pressure data from 18 stations within 100 km of Cabauw (Bosveld *et al.*, 2014a) ranged from 2.4–6 m s^{-1} during the SCM study periods. Furthermore, at the crossing level of 40 m as defined by Van de Wiel *et al.* (2012), wind speeds during the SCM study period were below the minimum 5 m s^{-1} to maintain continuous turbulence, so that the development of a very stable boundary layer is more likely. 2 m temperatures ($T_{2\mathrm{m}}$) decreased to 253.4 K, while at the 200 m level the diurnal cycle was hardly visible with temperatures of about 265 K, showing an absolute temperature gradient of almost 12 K over the 200 m. The snow depth in Cabauw was about 3.5 cm (averaged from the two stations closest by: Groot-Ammers, about 9 km from Cabauw (3 cm), and Benschop, about 6 km from Cabauw (4 cm)).

The snow heat flux was determined with $G = -\lambda\, \mathrm{d}T/\mathrm{d}z$, where we took the difference in temperature from the snow skin temperature determined from the long-wave radiation components and the observed ground-surface temperature below the 3.5 cm snow pack, over the 3.5 cm snow layer. For the conductivity λ, the value 0.021 W m^{-1} K^{-1} for fresh snow with a density of 100 kg m^{-3} was used, following Stull (1988). Note that, with this method, G can be underestimated for a large dz, since the temperature gradient in the snow is highly nonlinear and can be steeper close to the snow surface (Luce and Tarboton, 2001; Oldroyd *et al.*, 2013).

2.2. Sodankylä

The second case study is built on observations from the Arctic Research Centre of the Finnish Meteorological Institute (FMI–ARC, 2013), located at Sodankylä in northern Finland (67.36°N, 26.63°E). The area is fairly flat, though the land use is rather heterogeneous, with coniferous and deciduous forests (49%) alongside more open areas of peat bogs and shrub lands and a river close by (Batchvarova *et al.*, 2001; Atlaskin and Vihma, 2012).

A 48 m high micrometeorological mast in a Scots pine forest, having a moderate density of trees 10–12 m tall, measured temperature and relative humidity at heights of 3, 8, 18, 32 and 48 m and wind speed at heights of 18, 30, 38 and 47 m. An automatic weather station (AWS) in more open land located some 500 m from the weather mast provided data on air temperature and relative humidity at a height of 2 m and wind speed and direction at 10 m, as well as surface pressure. Comparing data from the two sites for our study period, the air temperatures at 2 and 3 m heights typically agreed within 0.5 K and the wind speeds at 10 and 18 m within 0.2 m s^{-1}. Furthermore, soundings were launched twice a day (0000 and 1200 UTC) at the AWS site and provided additional data on temperature, relative humidity, wind speed and direction in the vertical. Also the surface radiation fluxes (at the AWS site) and sonic anemometer based turbulent fluxes (at the mast) were measured.

The case study covered the night of 26–27 March 2009, when a low-pressure system was located east of Finland, as well as just north of the British Isles, with a weak pressure gradient over Finland (Figure 1(b)) resulting in weak wind speeds. Cloud-free conditions were observed with very low wind speeds of 0–1.5 m s^{-1} at the 10 m level (so somewhat intermittent) and between 0 and 2.7 m s^{-1} at 47 m at the top of the mast. The wind direction was mostly from the north to northwest. $T_{2\mathrm{m}}$ dropped from 269 K during the day on 26 March to 243 K at the end of the night on 27 March, while for the 48 m height this was 267.5 K during the day, which dropped to just over 252 K at night. Therefore, during the night a temperature inversion of over 9 K was reached between 2 and 48 m.

The observed snow depth was 62 cm. The snow heat flux G in this case was determined using the equation as for the Cabauw case, but on the basis of temperatures at the snow surface and at 60 cm snow depth above the soil (2 cm below the snow–atmosphere interface). For the conductivity λ, the value 0.084 W m^{-1} K^{-1} for snow with a density of 200 kg m^{-3} was used, following Stull (1988).

2.3. Halley

The third study location is the Halley research station of the British Antarctic Survey (75.58°S, 26.65°W) at the Brunt ice shelf in Antarctica. A micrometeorological mast provided temperature, relative humidity and wind speed and direction data at 1, 2, 4, 8, 16 and 32 m height. Also, the components of the radiation budget at the surface were available, as well as daily radiosonde data with information on temperature, relative humidity and wind speed and direction. For more information on the measurement site and observations, see e.g. King and Anderson (1988, 1994).

The study covered the cloud-free period starting at 8 h on 18 May 2003, when a strong stratification of 11 K between 1 and 32 m height was observed, which increased to 14 K after

9 h. A low-pressure system was located northeast of Halley, with a small high-pressure system to the west of Halley and another low-pressure system just over the Antarctic Peninsula (Figure 1(c)). Wind directions close to the surface ranged from south to southeast. Low wind speeds of 0–1.1 m s^{-1} at the 1 m level and 2.1–4.7 m s^{-1} at the 32 m level were observed.

Sonic anemometer data at 4, 16 and 32 m were available for the sensible heat flux. The latent heat flux (L_vE) was lacking, though this is usually very small at this site. The L_vE derived from bulk transfer relations (Garratt, 1992) was also around 0 (not shown here).

The snow depth estimation was more difficult than for the two other sites. As there is practically no snow melt, the snow density (ρ_{snow}) increases with depth and gradually transforms to ice due to pressure. For the SCM simulations, the snow depth as modelled by WRF–3D (6.2 cm) was applied.

The soil heat flux G was determined as for the Cabauw and Sodankylä cases, but now dT/dz was calculated using the surface temperature and a thermal diffusion model tuned to the buried thermometers. A conductivity $\lambda = 0.21$ W m^{-1} K^{-1} was used, which follows from the measured snow surface diffusivity (2.9×10^{-7} m^2 s^{-1}) and snow density (350 kg m^{-3}) and the heat capacity of the ice (2108 J kg^{-1} K^{-1}).

3. Model description and set-up

To evaluate the WRF single-column model (SCM), the full 3D model provided meteorological fields for the initial input files and the time-dependent advective forcings. This particular 3D run will be evaluated as well. In all cases, version 3.2.1 of the model was used.

3.1. 3D WRF

The WRF model is a mesoscale meteorological model that uses a vertically stretched σ coordinate with the model top set at a constant pressure. 60 vertical levels were applied here, with the highest resolution close to the surface. We used a nested approach, with horizontally 81 × 81 and 106 × 106 grid cells for the first and second domain, respectively, and a spatial resolution of 12 and 4 km, respectively. The centre points of the domains were set at the coordinates of the observational sites described in the section on observational data. The domains are shown in Figure 1. Furthermore, for the Sodankylä and Halley cases, polar stereographic projections were used, while a Lambert projection was used for Cabauw. Boundary conditions were provided by the European Centre for Medium-Range Weather Forecasts (ECMWF) operational analysis. The cases were run with a time step of 60 s.

For the 3D runs, the parametrization schemes were selected following the operational Antarctic Mesoscale Prediction System (NCAR UCAR, 2013). The BL physics were represented with the Mellor–Yamada–Janjic local, 1.5 order scheme (MYJ: Mellor and Yamada, 1982), for which the eddy diffusivities are determined utilizing the turbulent kinetic energy. The MYJ–BL scheme runs in conjunction with the eta-similarity surface-layer scheme (Skamarock *et al.*, 2008; Tastula and Vihma, 2011). For the long-wave and short-wave radiation, the Rapid Radiative Transfer Model for General Circulation Models (RRTMG: Iacono *et al.*, 2008) and Goddard scheme (Chou and Suarez, 1994) were used, respectively. For the microphysics, the WRF Single-Moment (WSM) five-class scheme was employed, while for the cumulus parametrization the Kain–Fritsch scheme was used (Skamarock *et al.*, 2008). Finally, the four-layer Noah land-surface model (LSM) was applied (Chen and Dudhia, 2001; Ek *et al.*, 2003). Note that different layer thicknesses in the WRF model are applied for land surfaces and sea-ice surfaces (Figure 2).

Considering that the thermal coupling is relatively important in the SBL for calm wind regimes (e.g. Sterk *et al.*, 2013), the surface characteristics should be captured accurately. To improve on the dominating land-surface characteristics of particular cases, we adjusted the threshold snow depth (SNUP, a threshold value in meter snow water equivalent: Ek *et al.*, 2003) that determines 100% snow cover, such that the modelled albedo matched the observed albedo. This is necessary because, with standard WRF settings, the snow cover remained unrealistically low for grassland, while it remained unrealistically high for an evergreen needle-leaf forest: for example, with the standard settings and 200 kg m^{-3} snow density (ρ_{snow}), 20 cm of snow is needed for 100% snow cover over grass, while 40 cm of snow is sufficient to have 100% snow cover over forest (Ek *et al.*, 2003). In reality, though the ground will be totally covered with snow, trees will stick through this snow cover (see Figure 2). By adjusting SNUP, a more realistic snow cover and albedo were obtained.

For the Cabauw case, we altered the SNUP value from 0.04 to 0.005 m, such that the resulting snow fraction obtained an albedo of around 0.63, as was observed. This SNUP value indicates that a snow layer of 5 cm is necessary to obtain 100% snow cover with a ρ_{snow} of about 100 kg m^{-3}, which was indeed found in the 3D model with fresh snow. The snow cover obtained was almost 80%. For the Sodankylä case study, the SNUP in 3D WRF was changed from 0.08 to 0.7 m, which resulted in an albedo of ∼0.42 and a snow cover of ∼0.54. For the Halley case, we could not retrieve the observed albedo, due to the fact that the short-wave radiation was absent during this part of winter. However, when sea ice is prescribed in the WRF–SCM runs, the snow cover is automatically set to 100%, so there was no need to change SNUP for this site.

Figure 3 shows the impact of the adjusted SNUP for both Cabauw (panels (a) and (b)) and Sodankylä (panels (c) and (d)) for the WRF–3D runs, using thick lines. For Cabauw, where the albedo with the old SNUP was about 0.3 with a snow cover of about 16%, there is a smaller isolating effect (larger snow heat flux G) of the snow layer, which results in higher 2 m temperature (T_{2m}) compared with the new SNUP run. For Sodankylä, with the old SNUP simulation, the albedo was about 0.67 with a snow cover of 98% (the maximum value with snow over land in WRF). This snow cover is unrealistically high when trees are present, and results in too low T_{2m} during the day. During the night, the old SNUP run is actually in better agreement with the observations regarding T_{2m} than the new SNUP run, although for the wrong reason, due to the unrealistically high snow cover.

3.2. WRF–SCM

The WRF–SCM is based on the WRF–3D model and uses the same physics and dynamics. Again, a vertically stretched σ coordinate was used for the vertical levels, but now 200 levels were applied, again with the highest resolution close to the surface, up to the model top at ≈12 km. We performed runs with similar physics to WRF–3D, but did additional runs with different BL and long-wave radiation schemes to test which scheme is more appropriate for the SBL modelling in the different case studies.

In addition to the MYJ–BL scheme, we applied the YSU–BL scheme (Hong *et al.*, 2006; Skamarock *et al.*, 2008; Hong, 2010), which is a first-order scheme (similar to Holtslag and Boville, 1993) where, for stable conditions, the eddy diffusivities are determined using the height, the boundary-layer depth and a velocity scale determined from the friction velocity and the stability function (Brost and Wyngaard, 1978; Troen and Mahrt, 1986). The YSU–BL scheme runs in conjunction with the MM5 surface-layer scheme (Skamarock *et al.*, 2008). Note that in the original WRF version 3.2.1 the stability function ϕ in YSU was erroneously implemented; this was corrected in the WRF 3.2.1 version that we use (S. Basu and W. Angevine, 2012; personal communication; see also Hu *et al.*, 2013; Sterk *et al.*, 2013). In this approach, mixing is reduced, though there are indications that in some cases the modelled BL has now become too stable (Sun and Barros, 2013). Furthermore, the limitation on the friction velocity (u_*) of 0.1 m s^{-1} to keep the heat flux from going to

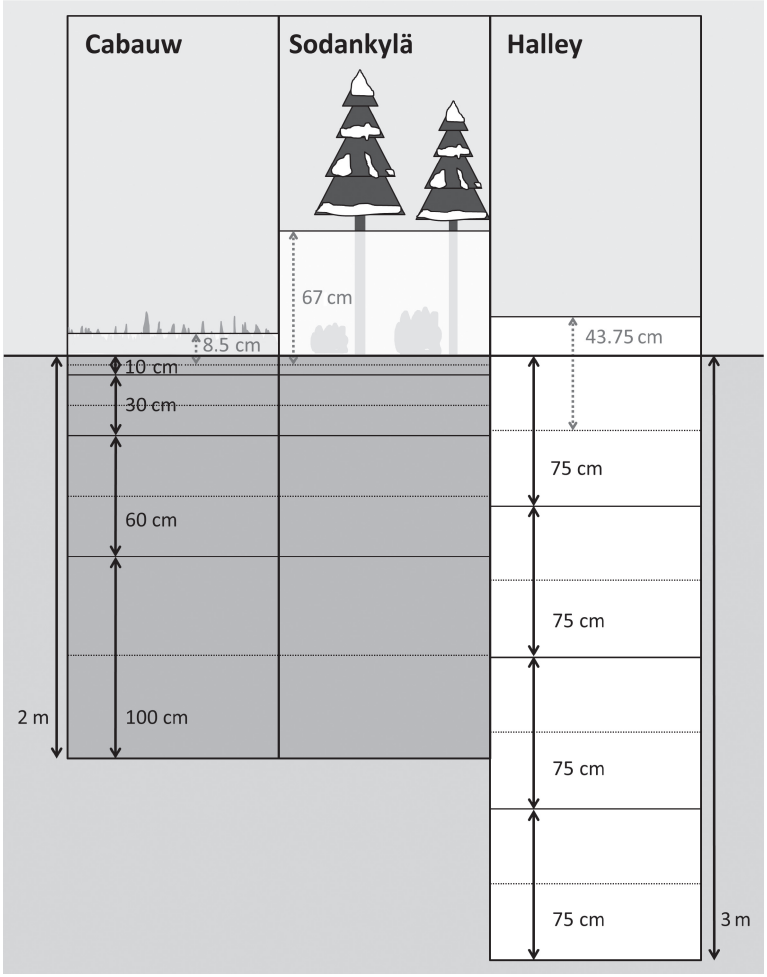

Figure 2. Illustration of the soil/ice layers in the Noah LSM for the three sites (not on scale). The black arrows indicate the standard thickness of individual layers. The actual depth of the layer for which calculations are performed is indicated by dotted lines. The grey dashed arrows indicate the top soil/ice layer when snow is present.

zero in very stable conditions has been lowered to 0.001 m s^{-1} following Jiménez *et al.* (2012).

In addition to the RRTMG long-wave (LW) radiation scheme, the ETA Geophysical Fluid Dynamics Laboratory (GFDL) and the NCAR Community Atmosphere Model (CAM) schemes were used. The differences between the LW radiation schemes are mostly in the amount of bands that they use and the molecular species that they treat (see Skamarock *et al.*, 2008).

Also for the WRF–SCM runs, we altered the value of SNUP (see section 3.1) for the Cabauw and Sodankylä cases. We did not use the same value as for the WRF–3D runs for the Cabauw case, because we applied a similar snow depth to the observed depth (3.5 cm), which is a bit larger than was found in WRF–3D (2.7 cm). This was due to the fact that the system in 3D WRF was located more westerly (∼50 km) than observed. We did use a similar ρ_{snow} of about 100 kg m^{-3} as was approximately modelled in WRF–3D (based on snow temperature and time: Ek *et al.*, 2003; Wang and Zeng, 2009) for the fresh snow at the start of the WRF–SCM study period. Then, with a SNUP of 0.006 m, we obtained a similar albedo to that observed, with a snow cover of around 0.83. Furthermore, for Cabauw the roughness length z_0 was adjusted from the grass/cropland value to the value of snow as used by WRF, i.e. 1 mm.

The new SNUP for Sodankylä amounted to 0.43 m, resulting in a snow cover of 0.55. A ρ_{snow} of 200 kg m^{-3} was now used, as was modelled approximately with WRF–3D at the WRF–SCM starting time. WRF–3D modelled a higher snow depth (97 cm compared with the observed 62 cm), but this bias was already present at the start of the run and originated from the boundary conditions provided by the ECMWF. The z_0 for evergreen needle-leaf forest remained unchanged (0.5 m); this is equal to the regional roughness length calculated for a 2 km × 2 km area surrounding Sodankylä at the end of winter (Batchvarova *et al.*, 2001).

For the Halley case, a ρ_{snow} of ∼200 kg m^{-3} was also modelled, which was implied in the WRF–SCM as well. For z_0, a value of 5.6×10^{-5} m was used, as measured at Halley for the momentum roughness length (King and Anderson, 1994).

Finally, we adjusted the vegetation fraction in the SCM. In WRF–3D, this was only 27.8% at Cabauw and 1% at Sodankylä. This vegetation fraction was determined from a spatially and monthly varying green vegetation fraction dataset determined with the satellite-derived global fields, which is interpolated to the correct day (Gutman and Ignatov, 1998; Ek *et al.*, 2003). However, we lack confidence in these values, since they are unrealistically low for the studied sites. In contrast, the ECMWF Integrated Forecasting System (IFS) applies a more realistic vegetation fraction of 0.85 for short grass and 0.9 for crops and mixed farming. Therefore we used a vegetation fraction of 0.85 in the WRF–SCM runs for Cabauw. At Sodankylä, according to Batchvarova *et al.* (2001), about 49% of the surrounding land is coniferous and deciduous forest. Although the IFS of the ECMWF operational model applies a vegetation cover of 90% for evergreen needle-leaf trees (ECMWF, 2013), we decided to use 49% in the current SCM runs, following Batchvarova *et al.* (2001), representing the heterogeneous nature of the Sodankylä environment.

Figure 3 depicts the effects of all the above-mentioned changes per step for the three sites. For the SCM no advection was prescribed and the WRF–3D new SNUP run was used to determine the initial profiles (see section 4: for Halley, SNUP was not changed, so the WRF–3D with the original SNUP was used for the SCM forcings). The grey lines in Figure 3 give the model results when all original values are used: snow depth from

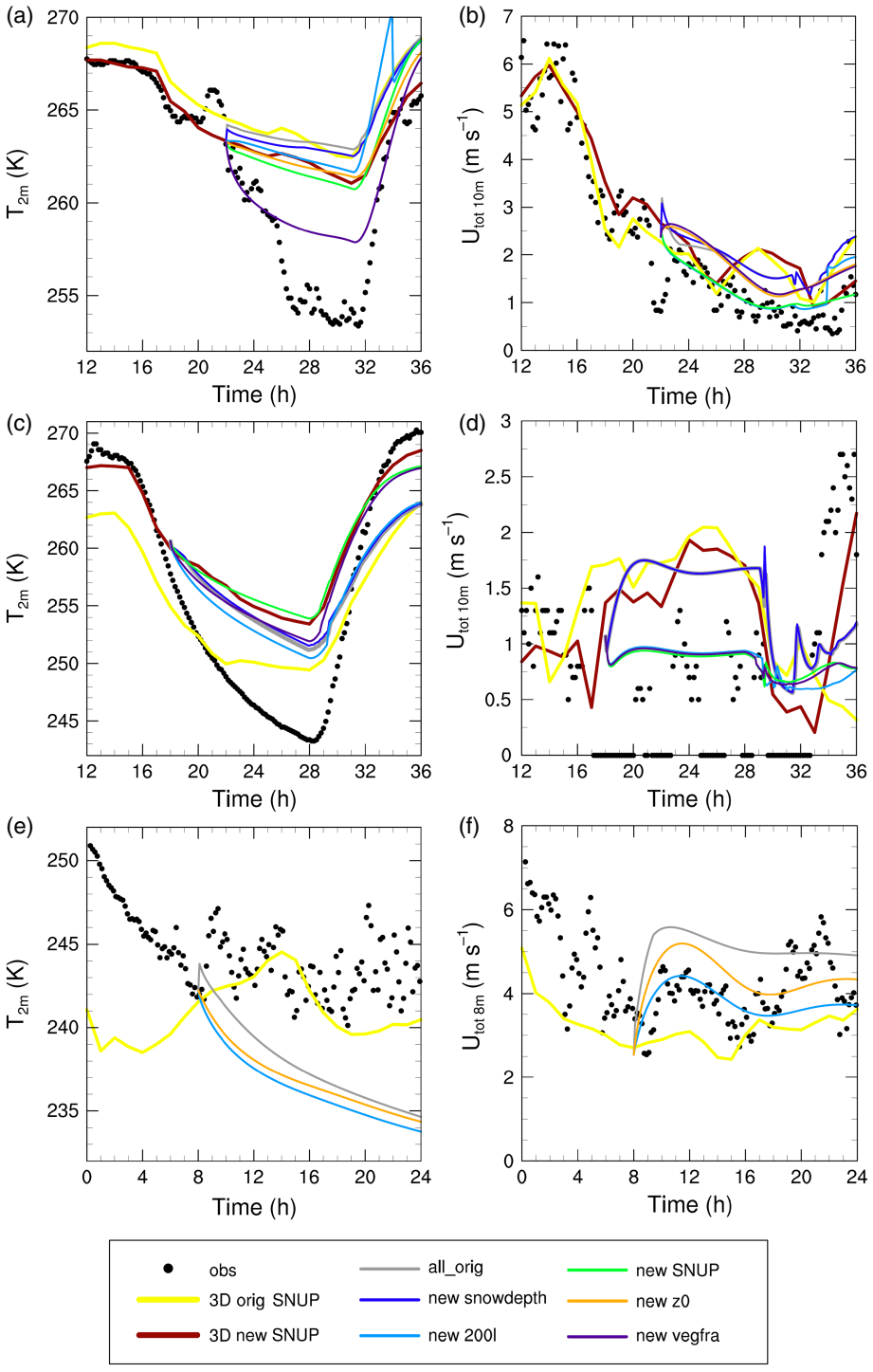

Figure 3. Time series for (a,c,e) 2 m temperature T_{2m} (K) and (b,d,f) 10/8 m wind speed $U_{tot\,10/8\,m}$ (m s^{-1}) for the (a,b) Cabauw, (c,d) Sodankylä and (e,f) Halley cases. Time series are given for the observations (obs), the WRF–3D run with both original and new SNUP values and the SCM runs with all original settings using the WRF–3D new SNUP run for the forcings (all_orig). For the other SCM runs, every time a new adjustment is added, starting with renewed snow depth following observations (new snowdepth, not for Halley), additionally increasing the vertical levels from 60 to 200 (new 200l), additionally adjusting SNUP (new SNUP, not for Halley), additionally adjusting the roughness length (new z0, not for Sodankylä), and additionally adjusting the vegetation fraction (new vegfra, not for Halley). All SCM runs are without advection, only using the initial profiles from the WRF–3D run with new SNUP values. See the text for further explanation.

WRF–3D, 60 vertical levels, original SNUP, original z_0, and the original WRF–3D vegetation fraction. Note that the other SCM runs have an additional (new) change each time, counting from top to bottom and left to right in the legend.

For Cabauw (Figure 3(a) and (b)), we find that the original SCM run is close to the WRF–3D runs, as the initial profiles from WRF–3D new SNUP were used, but with the original SNUP value. When the snow depth is increased to the observed value (dark blue line), G decreases and T_{2m} decreases and comes closer to observations, while wind speeds increase slightly with the higher snow cover. When, additionally, the number of vertical levels is increased from 60 to 200 (light blue line), T_{2m} decreases and improves even more (0.8 K lower at the end of the SCM study period (31 h)), while additionally the 10 m wind ($U_{tot\,10m}$) decreases and comes into close agreement with the observations. The sudden peak in T_{2m} just after sunrise (32 h) is explained by moisture distribution in a thinner layer with increased vertical resolution, which then increases the incoming long-wave radiation. The peak dissolves at 34 h, likely due to the increased wind speed at that time. The next step is to adjust SNUP for a more realistic higher snow cover (green line). This again reduces G and leads to an extra 1 K lower T_{2m} at 31 h. When z_0 is adjusted to fit the snow cover better (orange line), T_{2m} increases somewhat (0.6 K), though a lower skin temperature (T_{skin}) is found and thus a stronger temperature gradient close to the surface. Unfortunately $U_{tot\,10m}$ increases slightly (0.2–0.7 m s^{-1})

and is therefore less in agreement with observations, due to a stronger decoupling effect with smaller friction velocity (u_*). The last modification of increasing the vegetation fraction (purple line) has a strong impact on the SCM simulations. Due to the stronger isolating effect of the vegetation and hence smaller G, T_{2m} decreases strongly (an additional 3.5 K compared with the orange line) and comes into closer agreement with the observations.

For Sodankylä (Figure 3(c) and (d)), at first sight the adjusted parameters do not improve the SCM simulations and the original run (grey line) regarding T_{2m} is one of the better SCM runs compared with observations (though still almost 8 K too high at the end of the SCM study period (27 h)). However, this is due to the unrealistically high 98% snow cover. When the snow depth is lowered to 62 cm, which is observed (dark blue line), G increases and T_{2m} increases slightly further away from observations. When additionally the amount of vertical levels is increased (light blue line), as with Cabauw, T_{2m} decreases (an additional 1 K at 27 h) and $U_{tot\,10m}$ decreases; the latter, in particular, resembles observations more. Still, the snow cover is unrealistically high. To decrease the snow cover, the threshold value SNUP that determines 100% snow cover must be increased (green line) (while this had to be decreased for Cabauw). The decreased snow cover causes an increased G and again a higher T_{2m} (3.2 K higher at 27 h). Though this is now again further from observations, it does represent a more realistic snow surface for Sodankylä. As with Cabauw, an increase in vegetation (purple line) again has a positive effect on T_{2m}, as this decreases an extra 1.9 K at 27 h with the smaller G and becomes more in agreement with observations.

Finally, for Halley (Figure 3(e) and (f)), increasing the number of levels leads to similar model behaviour to the other cases: T_{2m} and $U_{tot\,8m}$ decrease. Additionally, lowering z_0 again increases T_{2m} and decreases T_{skin}, enhancing the temperature gradient at the surface, while, with a smaller u_* that is closer to observations, $U_{tot\,8m}$ increases as for Cabauw.

4. Methodology

This study emphasizes the evaluation of the WRF–SCM over a snow-covered surface for stable conditions. To compare SCM results with observations, we needed realistic input for the SCM. Studies often use a blend of observations and 3D model output to make an independent estimate of the required forcings (Baas *et al.*, 2010; Bosveld *et al.*, 2014a). Complete measurements to retrieve the atmospheric state are not always available and therefore we test whether the available set of WRF–3D fields provide reasonable forcings. Hence we will also evaluate one WRF–3D run per study case.

Regarding the SCM runs, we first performed a run without lateral forcings (set A). Next, we repeated the SCM runs where firstly only the geostrophic wind speed (U_g) changed in time (set B), secondly advection of momentum was added to the forcings in set B, otherwise known as the horizontal dynamical tendency of momentum (set C), and thirdly advection of θ and q was included in addition to set C (set D). Furthermore, SCM runs were performed where a form of data assimilation was applied above the BL height (set E). All time-varying parameters were updated every hour. For an overview of the various forcings, see Table 2.

In this evaluation, we used only 3D model output with the new SNUP value for Cabauw and Sodankylä and the output with standard SNUP for Halley (see section 3.1) to determine the forcings. Hereto, the thermodynamic profiles were linearly interpolated to the levels that serve as input for the SCM runs. The temperature and moisture profiles in the soil layers were taken from the 3D output directly, though the snow depth was taken from the observations to ascertain that surface characteristics are in better agreement with observations compared with the modelled snow depth.

Table 2. Overview of the particular forcing methods for the WRF–SCM runs.

Label	BL scheme	LW_{rad} scheme	Forcing
A	MYJ	RRTMG	No lateral forcings
B	MYJ	RRTMG	Varying U_g in time
C	MYJ	RRTMG	Varying U_g in time + momentum advection
D	MYJ	RRTMG	Varying U_g in time + θ, q, momentum advection
E	MYJ	RRTMG	Force to WRF–3D field above threshold height
D + YSU	YSU	RRTMG	Varying U_g in time + θ, q, momentum advection
D + GFDL	MYJ	GFDL	Varying U_g in time + θ, q, momentum advection
D + CAM	MYJ	CAM	Varying U_g in time + θ, q, momentum advection

U_g is generally a good approximation of the actual wind speed above the BL in extratropical synoptic-scale disturbances (Stull, 1988; Holton, 2004). Therefore, above a threshold height, we defined U_g as the actual wind speed modelled with WRF–3D. Note that with $U_g = \frac{1}{\rho f}\left|\frac{dp}{dn}\right|$, approximately the same values were obtained. Below this threshold, the geostrophic wind speed was kept constant to the wind speed at the threshold height. The threshold height has to be higher than the modelled BL height and also should not be located in the nose of the low-level jet (LLJ), to avoid too strong U_g close to the surface and therefore strong inertial oscillations. The BL height was determined following Troen and Mahrt (1986) when the bulk Richardson number reaches the critical value of 0.33, as used by Wetzel (1982) mainly for radiation dominated BLs (Vogelezang and Holtslag, 1996).

The advection prescribed in this study was determined by making use of the prognostic equations, where we neglected the molecular diffusion terms and applied the Boussinesq approximations (Stull, 1988):

$$\frac{\partial\overline{\theta}}{\partial t} = -\overline{U_j}\frac{\partial\overline{\theta}}{\partial x_j} - \frac{1}{\overline{\rho}c_p}\frac{\partial\overline{Q_j^*}}{\partial x_j} - \frac{L_vE}{\overline{\rho}c_p} - \frac{\partial(\overline{U_j'\theta'})}{\partial x_j}, \quad (1)$$

$$\frac{\partial\overline{q}}{\partial t} = -\overline{U_j}\frac{\partial\overline{q}}{\partial x_j} + \frac{S_q}{\overline{\rho}} - \frac{\partial(\overline{U_j'q'})}{\partial x_j}, \quad (2)$$

$$\frac{\partial\overline{u}}{\partial t} = -\overline{U_j}\frac{\partial\overline{u}}{\partial x_j} - f_c(\overline{v_g} - \overline{v}) - \frac{\partial(\overline{U_j'u'})}{\partial x_j}, \quad (3)$$

$$\frac{\partial\overline{v}}{\partial t} = -\overline{U_j}\frac{\partial\overline{v}}{\partial x_j} + f_c(\overline{u_g} - \overline{u}) - \frac{\partial(\overline{U_j'v'})}{\partial x_j}, \quad (4)$$

where θ is the potential temperature, U_j represents the component of the wind speed vector in direction j, ρ the air density, c_p the specific heat for dry air, Q^* the net radiation, L_vE the latent heat, q the specific humidity, S_q the net moisture source term for the remaining processes not already in the equation, u and v the u- and v-component of the wind speed respectively, f_c the Coriolis parameter and u_g and v_g the u and v components of the geostrophic wind speed, respectively. The variables with a bar indicate a mean value, variables with a prime indicate the turbulent fluctuation.

Here, the term on the left-hand side represents the tendency, the first term on the right-hand side represents advection and the last term on the right-hand side represents the turbulent flux divergence. The second and third terms on the right-hand side in Eq. (1) represent the radiative flux divergence and the change in temperature associated with latent heat release, respectively. In Eq. (2), $S_q/\overline{\rho}$ is the net source term for extra moisture processes. The second term on the right for the u and v equations is the geostrophic departure and is a combination of the terms for the influence of the Earth's rotation and the pressure gradient forces.

Above the previously mentioned threshold height, this is equal to 0. Note that in stationary conditions the advection terms are known to approximately balance the geostrophic departure term in the free atmosphere. Although, in our case, conditions are not stationary, it is clear that the u and v tendencies are very sensitive to all terms in the momentum equation and hence to the way they are prescribed for the SCM simulations.

Here, we determined the advection terms as a residual term from the other terms in the equation, using the WRF–3D results. We neglected the source term for additional moisture processes, because there was hardly any precipitation present (0.002 mm for Cabauw, 0.05 mm for Sodankylä and nothing for Halley in total for 9 h, as WRF–3D did simulate some clouds during some hours; see also the sections on the WRF–3D results). The tendencies at hour T_n were calculated based on the 3D results 1 h preceding (T_{n-1}) and 1 h following (T_{n+1}) hour T_n. For the other required terms on the right-hand side, we took the average of the preceding, current and the following hours.

In the additional set E, a form of data assimilation was applied above the BL height. This was achieved by relaxing the SCM state above the BL towards a prescribed 3D state on the advection time-scale (Ghan *et al.*, 1999; Rostkier-Edelstein and Hacker, 2010). In other words, the horizontal advective tendencies were obtained by the difference between the prescribed 3D field and the simulated SCM values over the advective time-scale to nudge the SCM simulation towards the WRF–3D field. The relaxation was only applied from a certain height above the BL upwards, to ascertain that the parametrizations in the BL are not affected. We used the same threshold height as for U_g mentioned above. We applied a smooth advective time-scale profile, in order not to stop the nudging at this height too abruptly. Above the threshold level, this was a small advective time-scale of 600 s, while it increased tangentially to 10 days over a range of 250 m below this threshold level.

5. Results

This section describes the model results for the three case studies over different terrains. For each case, we first discuss the WRF–3D results that formed the basis for the WRF–SCM forcing files (with adjusted SNUP for Cabauw and Sodankylä). Hereafter the WRF–SCM results are evaluated for sets A–E, as well as the runs with different BL and LW radiation schemes.

5.1. Cabauw

5.1.1. WRF–3D

The WRF–3D model was started at 0000 UTC on 3 February 2012. The first 12 h were considered as spin-up time and are not shown here. The 3D run represented T_{2m}, $U_{tot\,10m}$ and 2 m specific humidity (q_{2m}) well for the first 10 h (see Figure 4). However, WRF–3D was unable to capture the strong T_{2m} drop and remained too warm. Since wind speeds close to the surface were only slightly overestimated, we do not expect too large mixing due to excessive wind speeds to be the cause of this temperature bias. The WRF–3D runs did simulate some clouds at 24 and 25 h at around 400–800 m; however, we did not see an increase in the long-wave downward radiation ($LW\downarrow$) and therefore this may not explain the warm bias at the surface. Furthermore, $LW\downarrow$ was actually underestimated by $\sim$3–28 W m^{-2} during the SCM study period with WRF–3D. Note that the estimated accuracy of the measured $LW\downarrow$ is $\sim$4 W m^{-2} (Vihma *et al.*, 2009), though errors can be larger when frost, snow, rain or liquid condensate is present on the domes. Temperatures at 200 m deviated from the observations by at most 1 K and the wind-speed variations at this same height were followed nicely as well, though slightly underestimated by 2 m s^{-1} at the end of the night (not shown).

Concerning u_*, WRF–3D followed the available data rather well, but with an underestimation of about 0.05–0.1 m s^{-1}. The values were rather small, which is typical during calm winds. The wind-speed profiles were simulated reasonably well at most time steps (Figure 5). This also held for θ, but after 22 h only for the higher tower levels, because WRF–3D failed in reproducing the observed strong inversion.

The WRF–3D model produced a snowfall pattern that was located to the west (about 50 km) of the observed pattern, which showed a band of snowfall with a maximum depth generally in the north–south direction over the middle of the Netherlands. This partly explained the smaller snowfall than was observed at Cabauw (2.7 versus 3.5 cm), which affected the simulation of the near-surface temperature.

The BL modelled with WRF–3D was very shallow and always below 100 m for the SCM research period between 22 and 31 h. However, the threshold height to determine U_g should be not only above the BL, but also sufficiently high above the LLJ not to generate an unrealistic inertial oscillation when using this wind speed as U_g for the underlying model levels. A threshold depth of 400 m fulfilled the criteria nicely. The observed surface U_g (section 2.1, Table 1) is in good agreement with this derived U_g, thus supporting this method.

5.1.2. WRF–SCM

Here, results of our WRF–SCM experiments formulated in sets A–E are presented, followed by the experiment results with other BL and radiation schemes. All runs are with the snow depth as observed, 200 vertical levels, adjusted SNUP and z_0 and increased vegetation fraction (section 3.2). The runs were started at 22 h, when the situation became cloud-free, which is beneficial for the development of a very stable BL. Since we are mostly interested in the model performance during stable conditions, we will evaluate the WRF–SCM performance between 22 and 31 h (0700 UTC in the morning, just before sunrise).

The time series and vertical profiles after 31 h (the end of the night) in Figures 4 and 5 for the different forcing methods are indicated with sets A–E. The same parametrization schemes as in the WRF–3D run were used. Clearly, the 3D and SCM runs differ substantially for T_{2m} and q_{2m}. Mostly this was explained by the underlying medium and not, to a significant degree, the atmospheric forcings, as was explained in section 3.2. Due to the stronger and more realistic insulating effect accompanying the increased vegetation fraction, all these runs simulated a colder T_{2m} than WRF–3D, one closer to the observed T_{2m}, though the WRF–SCM was unable to capture the strong temperature drop around 26 h.

The differences for the T_{2m} simulations between sets A–E were rather small. Better results for T_{2m} were obtained when temperature and moisture advection were included (set D), decreasing the bias by about 0.8 K at 31 h compared with neglected advection (set A), while for the higher levels a slightly higher θ was simulated (up to about 0.6 K at 200 m), decreasing the bias here as well. Therefore, with set D, larger θ gradients were modelled. The temperature profiles showed that a varying U_g in time (set B) as well as momentum advection (set C) did not influence the temperature profile substantially. Also interesting was the profile of set E, where the profile above 400 m was nudged towards the WRF–3D field. Indeed, the higher levels followed the WRF–3D profiles, but this also influenced the profile below 400 m, where it appeared that the cold air could not be transported upwards and was therefore captured in the layer below, resulting in a stronger capping inversion just below 400 m that was not seen in the other runs. This trapping indeed appears to be caused by the nudging, as with an altered threshold height a similar model behaviour was found just below this threshold height (not shown).

The 10 m wind speed, $U_{tot\,10m}$, was modelled reasonably well, especially for set A. However, at higher levels the run went immediately through an inertial oscillation that disagreed with the higher level tower observations. This was especially clear with the hodograph at 80 m (Figure 4(e)), which was approximately

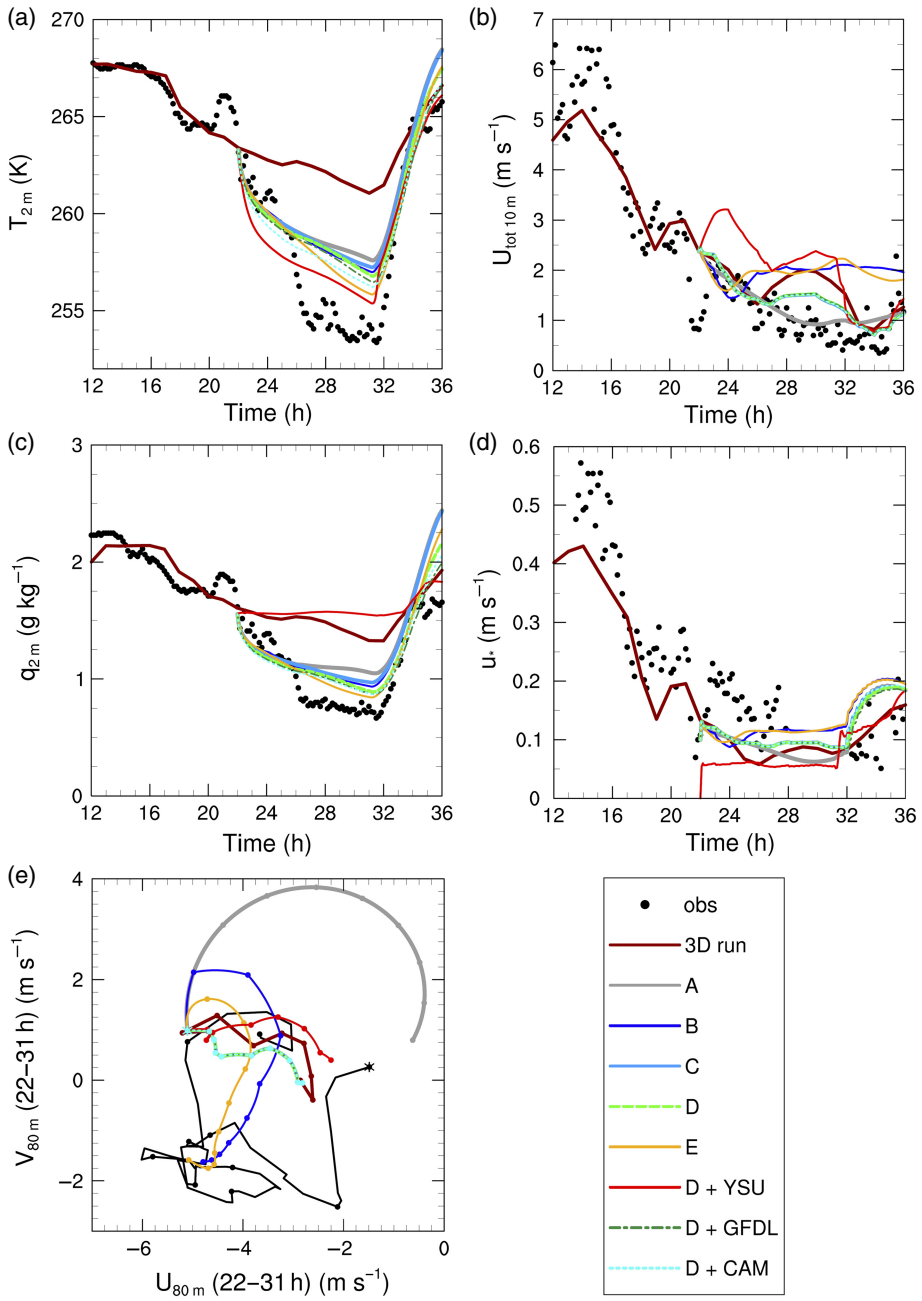

Figure 4. Time series for the Cabauw case for (a) 2 m temperature T_{2m} (K), (b) 10 m wind speed $U_{tot\,10m}$ (m s^{-1}), (c) 2 m specific humidity q_{2m} (g kg^{-1}), (d) friction velocity u_* (m s^{-1}) and (e) the hodograph at 80 m (wind speeds in m s^{-1}), where the asterisk indicates the time of the start of the WRF–SCM simulations (22 h). As the measurements are performed every 10 min, the SCM output is provided every 5 min and the WRF–3D output is provided hourly, only the full hours since the starting time are indicated with dots to show the progression in time. Time series are given for the observations (obs), the WRF–3D run (3D run), the WRF–SCM simulations for the different forcing methods (set A–E) and WRF–SCM with the YSU–BL scheme (D + YSU) and with various LW radiation schemes (D + GFDL, D + CAM).

the LLJ altitude of the observations, but also at other levels. Also, when U_g only was altered in time (set B), the modelled wind-speed profiles deviated a lot from reality, especially in the first few hours, though better agreement was found at hours 28–30. This also follows from the reduced mean bias error at 200 m (Table 3), though the biases increase at 10 m. Even further improvements were found when momentum advection was included as well (sets C–D): when compared with set A, biases were halved at 200 m. After 27 h, $U_{tot\,10m}$ remained slightly too high for sets C–D, though with ∼0.7 m s^{-1} this was reduced compared with ∼1–1.5 m s^{-1} for set B. Note that the set C and D runs overlapped mostly for the wind-speed simulations, indicating that θ and q advection did not really influence the wind simulations in this case. This was confirmed by the wind-speed profile at 31 h (and other hours, not shown here). These profiles also indicated that the momentum advection was very important in modelling the correct wind speed, though we must keep in mind that the LLJ is a dynamical phenomenon and hence simulations and observations may be in different phases at the time of the profile. However, studying the profiles at other hours by eye indicated that, overall, the sets with momentum advection yielded better wind-speed profiles (not shown). From the hodograph in Figure 4(e), we find that the observations do follow some inertial oscillation at 80 m. As mentioned before, this also holds for set A, though this is not at the correct magnitude. Sets B and E also go through an oscillation. This is not as clear for the runs with prescribed momentum advection that follow the WRF–3D results at 80 m more closely, which shows that the model is very sensitive to the advection term in Eqs (3) and (4). The oscillation is clearer with set C–D at other levels. Finally, with set E, also for wind speed, the nudging above the 400 m threshold level is felt by the underlying air, where an oscillation occurred right below this threshold height, possibly due to the fact that this layer could not transport its momentum upwards properly.

An analogous effect was found for the specific humidity (q) profiles (Figure 5), where, with set E, the SCM was forced to

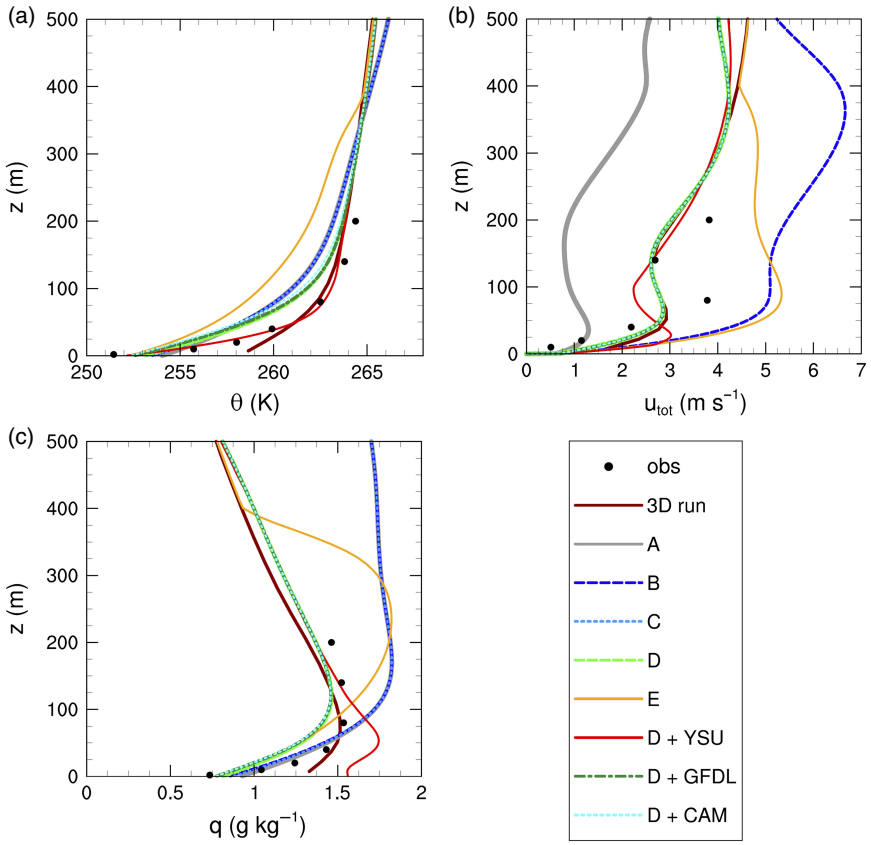

Figure 5. Vertical profiles for the Cabauw case at 31 h, after 9 h of WRF–SCM simulation, for (a) potential temperature θ (K), (b) total wind speed $U_{\rm tot}$ (m s^{-1}) and (c) specific humidity q (g kg^{-1}). (For an explanation of the legend, see Figure 4.)

a state with less q above 400 m, while in this way the moisture was kept in the layer below this height. The runs without any moisture advection corresponded to the tower data up to the 80 m level, though above that they remained too humid. With set D, the surface specific humidity was simulated better, but the run became somewhat too dry at higher levels up to 80 m, though the bias was decreased compared with sets A–C for even higher tower levels.

Regarding u_*, the WRF–SCM simulated this slightly higher than WRF–3D, but still a bit lower than observed at the start of the run and slightly too high after sunrise.

In summary, when we compare the runs with different forcings for this case over snow-covered grass in Cabauw for low wind speeds, it appeared that some form of advection is important. Without any advection, or only changing $U_{\rm g}$ in time, the runs deviate strongly from the observations and the WRF–3D field (though the latter is not free from errors either). This appeared to be very important for wind speed. Due to the fact that this was a low wind-speed case, turbulence is relatively weak and thus the turbulent flux divergence becomes relatively small and the other terms in Eqs (1)–(4) become relatively more important (Savijärvi, 2006, 2013). Also, when we compare the radiative flux divergence with the turbulent flux divergence in Eq. (1) for set D, we find for Cabauw close to the surface a turbulent flux divergence varying from $-1\,{\rm K\,h^{-1}}$ at the first hour to $-0.24\,{\rm K\,h^{-1}}$ at the end of the night, while the radiative flux divergence has a more continuous value of $\sim -0.15\,{\rm K\,h^{-1}}$, indicating the importance of radiative processes at these low wind speeds (Savijärvi, 2006, 2013). The advection is rather small close to the surface, but becomes relatively more important higher up. Moreover, we confirm that moisture advection was also very important and therefore we recommend applying advection for all variables, e.g. θ, q and momentum.

The SCM runs were repeated with the revised YSU–BL scheme (section 3.2). We performed the runs with all permutations (set A–E), as with the MYJ–BL scheme, however, the results for the five sets were similar to what we saw earlier. Thus we only show the YSU run with changing $U_{\rm g}$ and momentum, q and θ advection here (set D + YSU).

The $T_{2\rm m}$ behaviour is also simulated rather well with YSU: even lower temperatures were reached compared with MYJ. This increased the bias before 26 h and decreased the bias after this time. The stratification was represented better with a stronger exponential, or concave upwards, shaped profile (though this was too strong at the start of the run (not shown here)). This is interesting, since $U_{\rm tot\,10m}$ was strongly overestimated and it could be expected that this excessive wind speed will mix the BL more efficiently, leading to a weaker stratification. The LLJ was located at a lower altitude than with MYJ and too low compared with observations, though the observed 'S' shape in the wind-speed profiles was simulated as well (also, with MYJ, this 'S' shape vanished an hour later). Also u_* was somewhat lower compared with the other SCM runs, hinting at a possible decoupling effect. The magnitude of the sensible heat flux (H) decreased strongly compared with the MYJ runs and was closer to the observations, which also followed from the reduced bias (Table 3). Possibly the simulation was in the very stable regime, where H decreases with increasing stratification close to the surface (Holtslag *et al.*, 2007), which would again indicate a decoupling effect between the BL and the surface. Then the weaker turbulence would lead to reduced momentum loss to the surface, explaining the too-high wind speeds (Rinke *et al.*, 2012).

The latent heat flux ($L_{\rm v}E$) towards the surface, on the other hand, increased compared with the other SCM runs (around -10 compared with $-5\,{\rm W\,m^{-2}}$). This is explained by the larger amount of atmospheric moisture present within YSU, as was also found in the q profile and $q_{2\rm m}$ time series, for which it is seen that a humidity inversion does not really develop. Since q above $\sim$160 m was equal to q in set D, it is unlikely that this enhanced amount of q below this level for YSU is due to entrainment from higher levels. Since a clear temperature inversion does develop, a similar behaviour would be expected for humidity because the exchange coefficients in the surface layer and the eddy diffusivities

Table 3. Mean bias error (MBE), root-mean-square error (RMSE) and median of the absolute error between model simulations and observations, for the period of 22–31 h, for the Cabauw case for the following variables: 2 and 200 m temperature in K (T_{2m} and T_{200m}), 10 and 200 m wind speed in m s^{-1} ($U_{tot\,10m}$ and $U_{tot\,200m}$), 2 and 200 m specific humidity in g kg^{-1} (q_{2m} and q_{200m}), sensible (H) and soil heat flux (G) in W m^{-2}, net radiation in W m^{-2} (Q_{net}) and downward ($LW\downarrow$) and upward ($LW\uparrow$) long-wave radiation in W m^{-2}. Numbers in italic denote the run with the smallest bias between runs with various forcing methods (set A–D), those in bold the run with lowest bias between all WRF–SCM runs (based on multiple decimals).

		A	B	C	D	D + YSU	D + GFDL	D + CAM
MBE	T_{2m}	2.1	1.9	2.0	*1.8*	**0.4**	1.6	1.3
	T_{200m}	−0.6	−0.6	−0.6	*−0.3*	**−0.3**	−0.3	−0.4
	$U_{tot\,10m}$	***0.2***	0.6	0.4	0.4	1.2	0.4	0.4
	$U_{tot\,200m}$	−1.7	−0.9	*−0.8*	−0.8	**−0.7**	−0.8	−0.8
	q_{2m}	0.15	0.10	0.12	*0.08*	0.56	0.07	**0.06**
	q_{200m}	0.18	0.18	0.18	*0.05*	**0.05**	0.05	0.05
	H	*−16.9*	−16.9	−17.0	−17.0	**−5.8**	−17.7	−17.1
	G	−25.0	***−24.2***	−24.5	−25.3	−28.3	−26.2	−26.6
	Q_{net}	*−28.7*	−29.8	−29.4	−30.7	**−26.8**	−32.5	−31.6
	$LW\downarrow$	***−16.6***	−16.8	−16.7	−19.1	−19.1	−22.1	−21.7
	$LW\uparrow$	12.1	13.0	12.7	*11.6*	**7.6**	10.4	9.8
RMSE	T_{2m}	3.0	*2.7*	2.8	2.7	**2.0**	2.6	2.3
	T_{200m}	0.8	0.8	0.8	*0.5*	**0.4**	0.5	0.5
	$U_{tot\,10m}$	***0.3***	0.9	0.5	0.5	1.3	0.5	0.5
	$U_{tot\,200m}$	1.9	2.1	*1.0*	1.0	**0.9**	1.0	1.0
	q_{2m}	0.25	0.19	0.21	*0.19*	0.63	0.18	**0.18**
	q_{200m}	0.20	0.20	0.20	*0.10*	**0.10**	0.10	0.10
	H	*17.4*	17.4	17.5	17.5	**6.9**	18.2	17.6
	G	25.1	***24.2***	24.5	25.3	28.3	26.3	26.7
	Q_{net}	*29.1*	30.1	29.7	31.0	**27.2**	32.8	31.9
	$LW\downarrow$	***17.8***	17.9	17.8	20.0	20.0	22.8	22.6
	$LW\uparrow$	12.7	13.7	13.4	*12.3*	**8.7**	11.2	10.7
Median	T_{2m}	3.0	*2.6*	2.7	2.6	**1.9**	2.4	2.0
	T_{200m}	0.7	0.7	0.7	*0.5*	**0.4**	0.5	0.5
	$U_{tot\,10m}$	***0.2***	0.8	0.4	0.4	1.3	0.4	0.4
	$U_{tot\,200m}$	1.8	1.3	*0.9*	0.9	**0.8**	0.9	0.9
	q_{2m}	0.28	0.21	0.23	*0.20*	0.74	0.19	**0.19**
	q_{200m}	0.16	0.16	0.16	*0.09*	**0.09**	0.09	0.09
	H	18.1	*17.4*	18.3	18.3	**6.5**	19.0	18.2
	G	25.5	***24.3***	24.6	25.7	28.0	26.7	27.0
	Q_{net}	*28.3*	29.6	29.1	30.1	**26.1**	31.9	30.9
	$LW\downarrow$	***16.6***	16.8	16.8	18.6	18.4	21.7	21.2
	$LW\uparrow$	13.2	14.1	13.9	*12.7*	**8.8**	11.5	11.1

Note: for H these values are determined for the period of 22–26 h only, due to the erroneous measurements at later times. Measurements for L_vE were faulty for the entire period and therefore errors are omitted here. Set E is omitted here, due to the non-physical behaviour below the threshold height for relaxation towards the 3D field.

in the boundary layer are the same for both heat and humidity. This will be investigated in a future study.

The increase in L_vE with YSU was likely due to the increased wind speeds close to the surface, in combination with the larger moisture gradient between the surface and the 2 m level. The conductive heat flux (G) was a bit stronger at the start of the run (~ -37 W m^{-2} with YSU, compared with ~ -15 W m^{-2} with MYJ), due to the lower T_{skin}, and comparable to the other SCM runs from 26 h onwards.

Regarding the LW radiation schemes, both GFDL and CAM improved on the simulation of T_{2m} and q_{2m} by decreasing these values. However, this also resulted in lower values higher up, increasing the biases there. Unfortunately, the LW downward radiation ($LW\downarrow$), which was already underestimated, was now underestimated even more (Table 3). Therefore it appears that RRTMG performed best here. Similar results were seen for different LW radiation schemes in combination with YSU (not shown). Varying the radiation scheme did not seem to affect the wind field.

Overall, as long as the forcings are prescribed properly, both the MYJ and YSU–BL schemes perform reasonably well in simulating the SBL for this case over snow-covered grass. With YSU, the θ profiles are better forecasted than with MYJ, while with MYJ better wind profiles can be simulated. In a companion article, we perform a sensitivity analysis to study whether we can obtain similar improvements by adjusting the intensity of some of the governing processes in the SBL. Varying the LW radiation schemes led to smaller differences between the simulations, but RRTMG seems the better LW radiation scheme in that it underestimates $LW\downarrow$ the least.

5.2. *Sodankylä*

5.2.1. *WRF–3D*

The WRF–3D model was started at 0000 UTC on 26 March 2009. The 3D run performed very well for the first few hours (after the 12 h spin-up period) regarding T_{2m} and $U_{tot\,10m}$ (Figure 6), but, as for the Cabauw case, it remained too warm when the sun set. At this time also the observed $U_{tot\,10m}$ vanished, which was not captured by WRF–3D, though the modelled wind speed was mostly below 1.3 m s^{-1}. Compared with sounding observations at 0000 UTC on 27 March (6 h into the SCM simulation, Figure 7), near-surface temperatures remained too high, with the strongest biases close to the surface, and temperatures above 60 m were too low. This underlines that, as with Cabauw, the stratification was not strong enough. The LLJ was modelled at about the correct height at 6 h and with only a slightly lower magnitude; later, the LLJ was located a bit too high, with slightly stronger wind speeds than observed ($\sim$0.5 m s^{-1} too high). WRF–3D followed the sounding data above 100 m nicely for wind speed and was in good agreement with the tower data, though it missed the observed vanished winds at the lowest tower level.

The warm bias during night time could be partly explained by the overestimated q (Figures 6 and 7). Though q was also overestimated before night-time, the bias increased somewhat during the night. This also resulted in an overestimated $LW\downarrow$ ($\sim$1.5 W m^{-2} at the start and $\sim$7 W m^{-2} at the end of the SCM study period), while for Cabauw this was underestimated. This

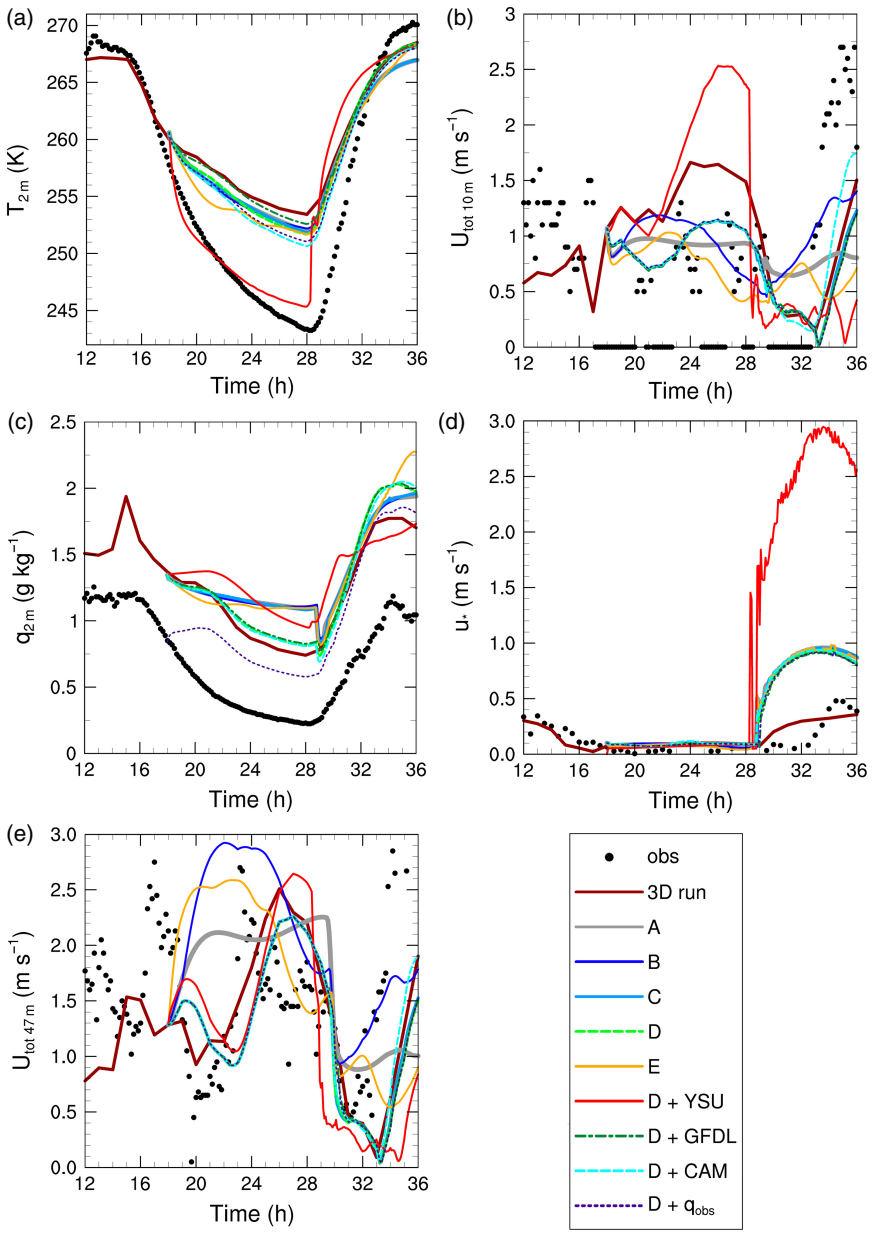

Figure 6. Time series for the Sodankylä case for (a) 2 m temperature T_{2m} (K), (b) 10 m wind speed $U_{tot\,10m}$ (m s^{-1}), (c) 2 m specific humidity q_{2m} (g kg^{-1}), (d) friction velocity u_* (m s^{-1}) and (e) 47 m wind speed $U_{tot\,47m}$ (m s^{-1}). Time series are given for the observations (obs), the WRF–3D run (3D run), the WRF–SCM simulations for the different forcing methods (set A–E), the WRF–SCM simulation with initial specific humidity profile based on observations (D + q_{obs}) and WRF–SCM with the YSU–BL scheme (D + YSU) and with various LW radiation schemes (D + GFDL, D + CAM).

overestimated $LW\downarrow$ may also be related to the low clouds that were modelled for the lowest model levels for 2000–2300 UTC and for 2000 UTC the next day. For other time steps, the cloud fraction was 0 or below a fraction of 0.1. We see a slight increase in $LW\downarrow$ at 20 h, but this decreases again right after that. However, for clear skies, $LW\downarrow$ was also overestimated (∼1.5–5 W m^{-2} in the 6 h prior to the SCM study period), making it unlikely that the present clouds are the main contributor to the overestimated temperatures close to the surface, as these were modelled better in the 6 h prior to the SCM study (Figure 6(a)).

The BL was very shallow during the night, as the critical Richardson number was already reached below the first model level. The friction velocity u_* was around 0.1 m s^{-1}, slightly higher than the available measurements. As a threshold height for U_g for the SCM runs, the 300 m height was chosen, which is located sufficiently above the LLJ and the BL height.

5.2.2. *WRF–SCM*

Next, WRF–SCM results are presented for the Sodankylä case for sets A–E and the runs with different BL and radiation schemes (Figures 6 and 7). All runs are with the snow depth as observed, 200 vertical levels, adjusted SNUP and increased vegetation fraction (see section 3.2). The period of interest was from 1800 UTC on 26 March 2009, which was the first hour after sunset, until 0300 UTC (27 h) the next day, which was just before sunrise. During this time, stable conditions were observed along the tower.

T_{2m} modelled with the WRF–SCM was improved compared with WRF–3D by a few K, depending on the forcings, resulting in a stronger θ gradient. Differences between sets A–D were small close to the surface, though, higher up in the θ profile, slightly lower temperatures (∼0.7 K at 60 m) were found for set D compared with sets A–C. Even better T_{2m} was obtained with set E; however, the artificial inversion below the threshold height of 300 m was again present, as with the Cabauw case, though less strong.

For wind, again differences close to the surface were small (Figure 6(a)), though now large differences between the sets were found at higher levels (Figures 6(e) and 7(b)). As for Cabauw, prescribing advection strongly impacts the simulated wind speed. Regarding the profiles in Figure 7(b) at 0000 UTC, results from sets C–D were in better agreement with the sounding data, compared with sets A–B. At least between 100 and 400 m,

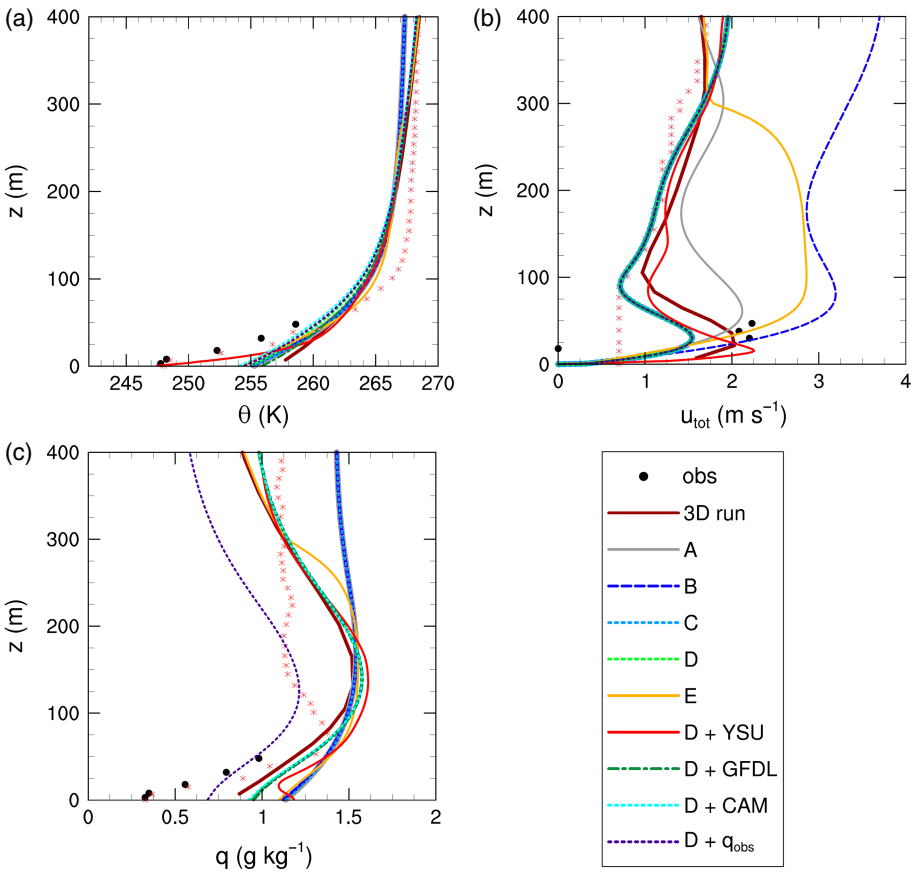

Figure 7. Vertical profiles for the Sodankylä case at 0000 UTC, 6 h into the WRF–SCM simulation when sounding data were available, for (a) potential temperature θ (K), (b) total wind speed U_{tot} (m s^{-1}) and (c) specific humidity q (g kg^{-1}). (For an explanation of the legend, see Figure 6; sounding data are indicated with red asterisks.)

the biases between sets C–D and observations were within 0.25 m s^{-1}, while they reached up to 1.2 m s^{-1} for set A and up to even 2.5 m s^{-1} for set B, supporting the supposition that prescribing proper momentum advection was necessary. At this particular time, sets C–D underestimate the higher level tower data compared with the other sets, though the general bias over 9 h at 47 m decreases somewhat (Table 4) and indeed a better agreement with the tower data for sets C–D is seen at other times (not shown).

For Sodankylä, information about the wind direction and thus the wind components was unavailable for the tower levels. To evaluate the model skills for higher level wind speeds, the 47 m wind speed ($U_{tot\,47m}$) time series are shown in Figure 6(e), instead of the hodograph. This figure also indicates that prescribing momentum advection was beneficial for the WRF–SCM simulation, especially for the first hours of the simulation, which already followed from the decreased biases between model runs and observations at 47 m (Table 4).

Part of the explanation for the overestimated temperature is the overestimated q, as already found with WRF–3D. It is interesting that lower temperatures were found with WRF–SCM compared with WRF–3D, but q was overestimated even more. These lower temperatures could be explained by the smaller G found with WRF–SCM compared with WRF–3D, due to the adjusted surface characteristics, such that heat was less easily transported from the deeper soil layers to the surface. Prescribing moisture advection was beneficial for q_{2m} and the q profiles, in comparison with not prescribing it.

Interestingly, $LW\downarrow$ was not too far off, with a mean bias error (MBE) of ∼4.3 W m^{-2} (slightly overestimated; for Cabauw this was underestimated), even though q was strongly overestimated. This again may point to a deficiency in the LW radiation scheme. According to Zhang *et al.* (2001) and Svensson and Karlsson (2011), the clear-air $LW\downarrow$ is more sensitive to small changes in the q profile for cold and dry conditions than for warm and humid conditions. Consequently, q is then very important for the radiation balance at the surface. When we prescribed the initial moisture profile from the average of the soundings at 1130 and 2330 h on 26 March and the lower tower levels, to test the sensitivity of the WRF–SCM runs to the initial set-up of the moisture, the run started with a correct q_{2m} but immediately tried to regain a balance by increasing q_{2m}. Furthermore, q was underestimated at higher levels compared with the sounding data (Figure 7). We did see a positive effect of lower q in the decreased θ and about 1 K lower T_{2m} at the end of the night. Also, now the $LW\downarrow$ bias has decreased compared with the D run and has become very small (Table 4). Again, we point out that this may be for the wrong reasons, since q was overestimated below about 40 m and underestimated at the higher levels.

When we again compare the radiative and turbulent flux divergence from Eq. (1) for set D to study the effect of the radiative processes, we see that the radiative flux divergence can reach up to −4 K h^{-1} at the start of the run, which decreases to ∼ −2.3 K h^{-1} at 9 h. For the turbulent flux divergence, this is ∼ 2.4–1.9 K h^{-1} at 1 and 9 h respectively. This is now positive, as was also found in Tjemkes and Duynkerke (1989), due to that turbulence has to warm the layer close to the surface, since the radiative cooling is much larger than the total cooling rate in the BL. Indeed, at higher levels, negative values for both components are found. Both processes are of comparable magnitude, which again shows the importance of the radiative processes.

Runs were repeated with the revised YSU–BL scheme with time-changing U_g and momentum, q and θ advection. Strong differences are seen compared with MYJ. With YSU, T_{2m} biases were greatly reduced (despite the even stronger overestimated q), while temperature biases increased for the highest two tower levels, with simulated temperatures being too high. Therefore, YSU was able to generate a very stably stratified BL, which in fact became somewhat too stable, as was found for the first few hours with the Cabauw case and in previous research (Sun and Barros,

Table 4. Mean bias error (MBE), root-mean-square error (RMSE) and median of the absolute error between model simulations and observations, for the period 18–27 h, for the Sodankylä case for the following variables: 2 and 48 m temperature in K (T_{2m} and T_{48m}), 10 and 47 m wind speed in m s^{-1} ($U_{tot\,10m}$ and $U_{tot\,47m}$), 2 and 48 m specific humidity in g kg^{-1} (q_{2m} and q_{48m}), sensible (H), latent (L_vE) and soil heat flux (G) in W m^{-2}, net radiation in W m^{-2} (Q_{net}) and downward ($LW\downarrow$) and upward ($LW\uparrow$) long-wave radiation in W m^{-2}. Numbers in italic denote the run with the smallest bias between runs with various forcing methods (set A–D), those in bold the run with the lowest bias between all WRF–SCM runs (based on multiple decimals, D + q_{obs} is not included).

		A	B	C	D	D + q_{obs}	D + YSU	D + GFDL	D + CAM
MBE	T_{2m}	6.4	*6.3*	6.4	6.4	5.9	**0.2**	7.1	5.7
	T_{48m}	0.7	0.7	0.7	***0.1***	−0.1	1.1	0.4	−0.3
	$U_{tot\,10m}$	*0.6*	0.7	0.6	0.6	0.6	1.4	**0.6**	0.6
	$U_{tot\,47m}$	0.6	1.1	0.1	*0.1*	0.1	0.2	**0.1**	0.1
	q_{2m}	0.75	0.74	0.75	*0.64*	0.36	0.81	0.65	**0.63**
	q_{48m}	−3.45	−3.45	*−3.45*	−3.51	−3.80	**−3.44**	−3.51	−3.52
	H	*−16.7*	−17.0	−16.8	−16.8	−18.0	**−13.8**	−15.8	−17.4
	L_vE	−2.1	−2.1	−2.1	*−1.9*	−1.4	−5.8	**−1.8**	−2.0
	G	−1.0	*−1.0*	−1.0	−1.0	−1.7	−1.5	**−0.2**	−1.5
	Q_{net}	18.1	*17.8*	18.0	18.2	16.5	18.2	20.4	**16.9**
	$LW\downarrow$	4.3	*4.2*	4.3	4.5	−1.1	1.9	11.5	**0.5**
	$LW\uparrow$	−12.6	*−12.5*	−12.5	−12.6	−16.5	−15.1	**−7.7**	−15.3
RMSE	T_{2m}	6.6	*6.5*	6.6	6.6	6.1	**1.1**	7.4	5.8
	T_{48m}	2.0	1.9	2.0	*1.7*	1.6	2.3	1.9	**1.5**
	$U_{tot\,10m}$	***0.8***	0.9	0.8	0.8	0.8	1.5	0.8	0.8
	$U_{tot\,47m}$	0.9	1.4	0.7	*0.7*	0.7	0.8	**0.7**	0.7
	q_{2m}	0.76	0.75	0.76	*0.64*	0.37	0.82	0.66	**0.64**
	q_{48m}	3.66	3.66	*3.66*	3.68	3.95	**3.62**	3.68	3.69
	H	*16.9*	17.2	17.0	17.0	18.2	**14.3**	16.0	17.7
	L_vE	2.1	2.2	2.2	*1.9*	1.5	5.8	**1.8**	2.0
	G	4.2	4.2	4.3	*4.2*	4.3	4.1	**4.0**	4.3
	Q_{net}	19.2	*18.9*	19.2	19.4	17.8	19.2	21.7	**18.2**
	$LW\downarrow$	4.5	*4.4*	4.5	4.6	1.6	2.1	11.6	**1.1**
	$LW\uparrow$	14.7	14.5	14.8	*14.5*	17.9	16.3	**10.2**	16.9
Median	T_{2m}	6.8	*6.6*	6.9	7.0	6.6	**0.9**	7.9	6.2
	T_{48m}	1.7	1.7	1.8	*1.4*	1.3	2.3	1.7	**1.2**
	$U_{tot\,10m}$	0.9	0.9	0.7	*0.7*	0.8	1.2	**0.7**	0.7
	$U_{tot\,47m}$	0.7	1.1	0.6	*0.6*	0.6	**0.5**	0.6	0.6
	q_{2m}	0.80	0.79	0.81	*0.62*	0.37	0.83	0.64	**0.62**
	q_{48m}	3.27	3.28	*3.27*	3.33	3.62	**3.23**	3.32	3.33
	H	*16.3*	17.1	16.5	16.5	17.7	**13.1**	15.5	17.5
	L_vE	2.2	2.2	2.2	*1.9*	1.5	5.8	**1.8**	2.0
	G	3.0	3.0	3.1	*3.0*	2.8	**2.8**	3.2	2.8
	Q_{net}	16.6	*16.0*	16.8	16.7	15.1	16.6	18.9	**15.8**
	$LW\downarrow$	4.4	*4.3*	4.4	4.8	0.7	2.0	11.5	**1.0**
	$LW\uparrow$	10.6	*10.1*	10.7	10.9	14.8	13.6	**5.8**	13.9

Note: Set E is omitted here, due to the non-physical behaviour below the threshold height for relaxation towards the 3D field.

2013; Kleczek *et al.*, 2014). As for Cabauw, stronger near-surface wind speeds were simulated with YSU and biases increased. Again, a stronger LLJ at a lower altitude was modelled, which was for most time steps too strong and at too low an altitude (up to 1.5 m s^{-1} too fast and up to 20–40 m too low), but the sharpness of the LLJ nose was in better agreement with observations than with the SCM runs with MYJ. Furthermore, a strong shift was observed around 28 h, where T_{2m} increased strongly and wind speeds decreased strongly. At this time the sun rises, resulting in a lot of mixing and a dilution of the strong stratification, which is more efficient with YSU. This also explained the increase in u_* after this time.

The runs with set D were also repeated with two different LW radiation schemes (D + GFDL and D + CAM). With GFDL and CAM, higher and lower temperatures were obtained, respectively, than with set D and the RRTMG LW radiation scheme, while for the Cabauw case both schemes simulated lower temperatures. Apparently, these schemes handle these challenging conditions with low q differently from the Cabauw case. Very minor differences were found in q_{2m} and the q profile; however, the $LW\downarrow$ bias increased and decreased for GFDL and CAM respectively, compared with the case when RRTMG was used. In fact, $LW\downarrow$ modelled with CAM was in good agreement with the observations during the night, though overestimated after sunrise, despite the already overestimated q. The influence of the LW radiation scheme on the wind-speed simulations was again negligible.

5.3. *Halley*

5.3.1. *WRF–3D*

The WRF–3D model was started at 0000 UTC on 15 May 2003. The SCM study started at 8 h on 18 May 2003, therefore the spin-up time for the Halley case was longer than for Cabauw and Sodankylä. However, this may be necessary due to the limited observations in this area and thus limited influence of observations on the ECMWF boundary conditions, so that the model may require more time to reach equilibrium with the underlying medium. Time series are shown from 0 h on 18 May 2003 onwards, assuming 72 h spin-up.

Initially, WRF–3D underestimated T_{2m} (Figure 8), from the starting time of the WRF–SCM simulations onwards, this recovered and observations were followed better, though underestimations of up to ∼5 K were found. The wind-speed variation at the 8 m level ($U_{tot\,8m}$) was followed accurately by the WRF–3D model as well, but $U_{tot\,8m}$ was slightly underestimated with 0–3 m s^{-1}.

Modelled profiles after 9 h of simulation (Figure 9) indicated an underestimation of the temperature inversion for Halley, consistent with the results for Cabauw and Sodankylä. The near-surface θ matched well, but θ at 32 m was modelled almost 8 K too low. Regarding the wind-speed profiles, we found that the order of magnitude was in agreement with the observations, although the LLJ observed at 10 m height was not reproduced with WRF–3D

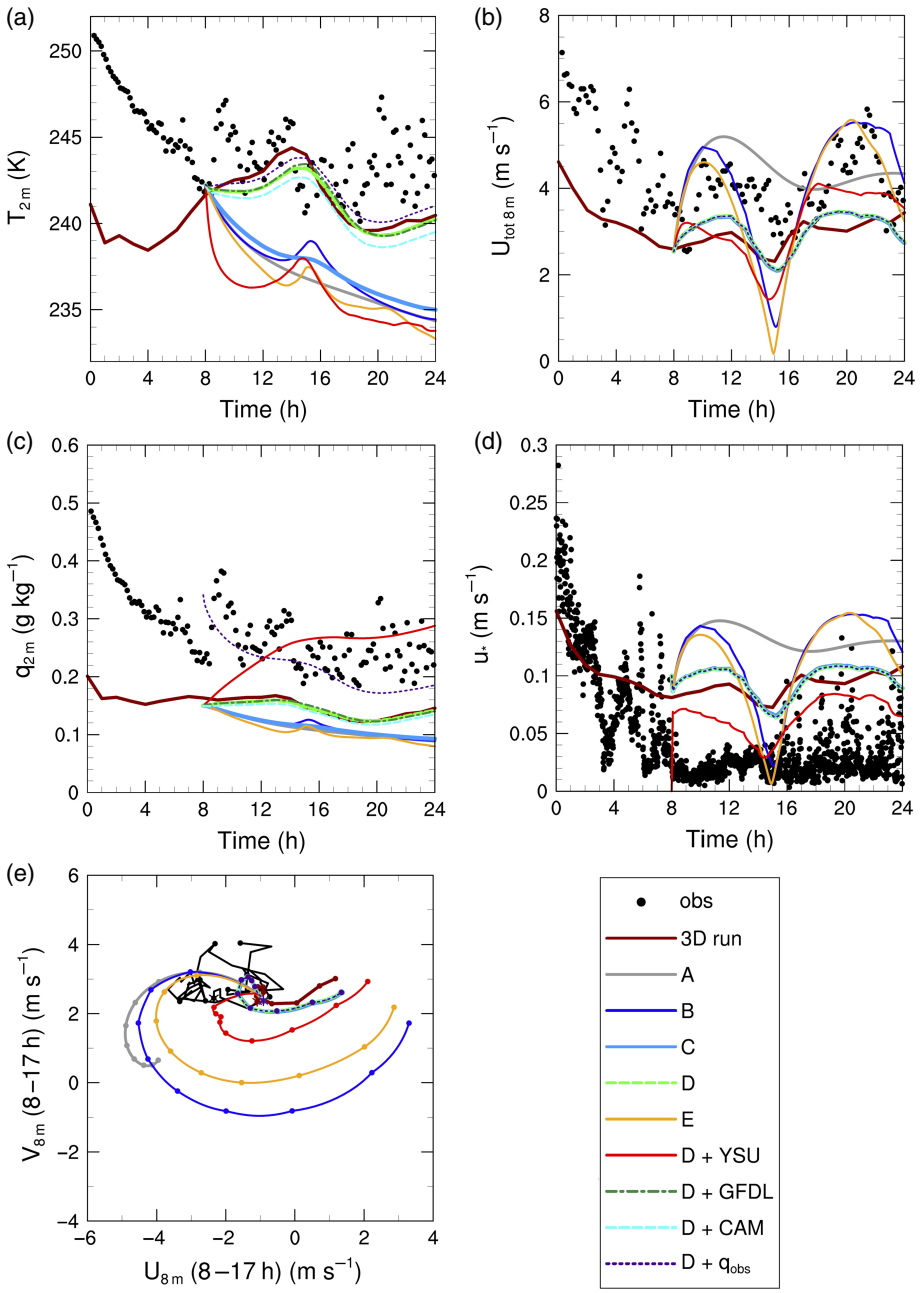

Figure 8. Time series for (a) 2 m temperature T_{2m} (K), (b) 8 m wind speed $U_{tot\,8m}$ ($m\,s^{-1}$), (c) 2 m specific humidity q_{2m} ($g\,kg^{-1}$), (d) friction velocity u_* ($m\,s^{-1}$) and (e) the hodograph at 8 m (wind speeds in $m\,s^{-1}$), where the asterisk indicates the time of the start of the WRF–SCM simulations (8 h). As the measurements are performed every 10 min, the SCM output is provided every 5 min and the WRF–3D output is provided hourly; only the full hours since the starting time are indicated with dots to show the progression in time. Time series are given for the observations (obs), the WRF–3D run (3D run), the WRF–SCM simulations for the different forcing methods (set A–E), the WRF–SCM simulation with the initial q profile based on observations (D + q_{obs}) and WRF–SCM with the YSU–BL scheme (D + YSU) and with various LW radiation schemes (D + GFDL, D + CAM).

at this time step. At other time steps, the LLJ was reproduced (not shown) but at too high an altitude (about 30–60 m).

The cold bias may be explained by, amongst other things, too low q_{2m} (0.05–0.2 $g\,kg^{-1}$) and q at the higher levels. With a modelled amount of 0.18 $g\,kg^{-1}$ at 32 m, the model did not even contain half the observed q (0.43 $g\,kg^{-1}$). Note that the sounding at 3 h after the start of the WRF–SCM simulation indicated a q of ~0.35 $g\,kg^{-1}$ at around 150 m, which decreased to 0.31 $g\,kg^{-1}$ at 500 m, for which the WRF–3D run simulated 0.23 and 0.29 $g\,kg^{-1}$ respectively, hinting at a better representation higher up. Unfortunately, only one sounding per day was available, so that we could not compare model results with observations higher than 32 m at other time steps. Though there were some clouds modelled at around 5 and 8 km, $LW\downarrow$ was underestimated with ~23–30 $W\,m^{-2}$. We expect the clouds to have a minor influence on the SCM simulations in this case, since SCM results in which clouds were kept absent had a similar amount of $LW\downarrow$.

The modelled BL was very shallow and varied between 20 and 40 m during the WRF–SCM study period. The modelled u_* followed the observed decrease accurately just before the start of the WRF–SCM simulations, but remained too high later on (0.07–0.11 $m\,s^{-1}$ versus the observed 0.01–0.08 $m\,s^{-1}$ (excluding some spikes)). As a threshold height for U_g used in the WRF–SCM simulations, the 300 m height was chosen, which again was located sufficiently above the BL height and the LLJ.

5.3.2. *WRF–SCM*

Here, WRF–SCM results for Halley, for sets A–E and the runs with different BL and radiation schemes, are described (Figures 8 and 9). The evaluation period ranged from 8 to 17 h on 18 May 2003 and was characterized by stable conditions and low wind speeds. Since the episode covered a polar night, we decided to keep the study period 9 h, i.e. equal to those for Cabauw and Sodankylä.

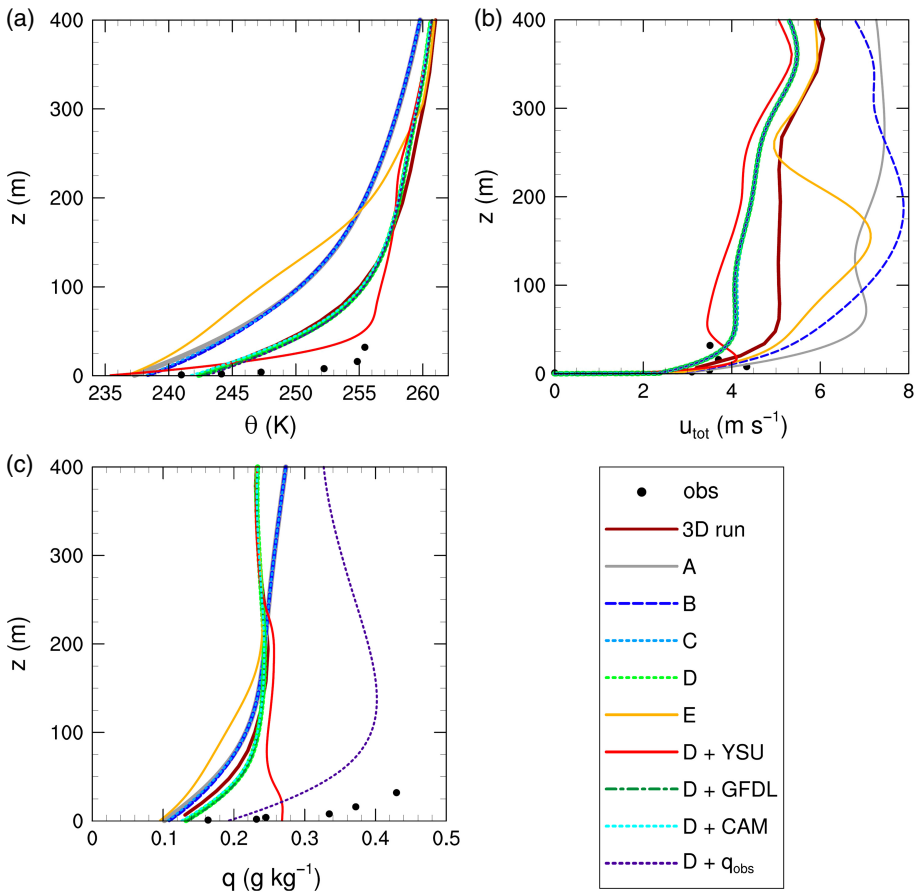

Figure 9. Vertical profiles for the Halley case at 17 h on 18 May 2003, 9 h into the WRF–SCM simulation, for (a) potential temperature θ (K), (b) total wind speed U_{tot} (m s^{-1}) and (c) specific humidity q (g kg^{-1}). (For an explanation of the legend, see Figure 8.)

WRF–3D modelled the surface conditions as sea ice with 100% snow cover for 6.2 cm of snow, which had $\rho_{snow} \approx 200\,\mathrm{kg\,m^{-3}}$. This was applied in the WRF–SCM as well, since it is difficult to determine the actual observed snow depth due to the gradual transition from snow to firn to ice in those regions. Though Halley is in reality located on an ice shelf of about 100 m, we do not expect a large influence of the underlying ocean boundary at 3 m depth (the standard sea-ice depth used in WRF) at this time-scale. We furthermore adjusted the z_0 of the snow to 5.6×10^{-5} m, as was measured at the Halley location (King and Anderson, 1994).

In contrast to results for Cabauw and Sodankylä, the T_{2m} results deteriorated with the WRF–SCM for Halley. The cold bias already modelled with WRF–3D increased even more, the extent depending on the forcing type. Without temperature advection (set A–C), we noticed a runaway cooling effect for which the simulated T_{2m} deviated more and more from reality, up to 6 K after 9 h. When temperature advection was prescribed (set D), T_{2m} was fairly similar to the 3D output, though about 1 K lower for the first few hours. The θ profiles also benefited from the prescribed θ advection, since the near-surface θ of set D was more in agreement with observations. At the highest tower level, θ remained underestimated by ∼8 K with set D, though this bias was reduced from an underestimation of ∼13 K with set A–C. For all forcing types, the θ inversion remained too weak compared with the observations, though with set D the inversion became slightly stronger. Also, with set E T_{2m} remained too low and, as for the other cases, the artificial inversion was modelled in the θ profile.

For wind speed, similar results to those for WRF–3D were found, with set D in the $U_{tot\,8m}$ time series, and for set B and E strong oscillations were simulated, which after around 17 h actually matched the order of magnitude of the observed $U_{tot\,8m}$ nicely, though in our study period the strong decrease was not observed. Though biases did not differ much at 8 m (Table 5), they decreased greatly at 32 m (and 2 m, not shown) with prescribed momentum advection. This was confirmed by the wind profiles (Figure 9(b) and at other hours, not shown), and by the hodograph for 8 m which is approximately the LLJ height of the observations (Figure 8(e)), where the wind-speed magnitude for set C–D was in the range of what was observed. This holds even more so for 2 and 32 m (not shown). Again, for set E, the model felt the restriction at the 300 m level in the wind-speed profile.

Considering q_{2m}, the WRF–SCM was too dry and the deficiency increased when moisture advection was absent. The q profile also showed a strong underestimation and too weak a moisture inversion. Slightly higher q values were found up to 130 m for set D; not prescribing q advection leads to even lower q compared with WRF–3D. To test the sensitivity of the WRF–SCM to the initial q profile, we performed an additional simulation with an initial q profile based on a linear interpolation in time between the soundings on 17 and 18 May 2003, combined with the tower data. This showed a clear improvement in q_{2m} (mean bias error decreased from −0.11 to $-0.03\,\mathrm{g\,kg^{-1}}$, see Table 5) and a slight improvement for T_{2m} (mean bias error decreased from −1.4 to −0.9 K). Although the moisture inversion strength was still underestimated, it was modelled better than when using the WRF–3D initial q profile. Biases in Table 5 also indicated improvements in temperature and humidity along the tower. Changes in the wind simulations were negligible.

Also for Halley, we compared the radiative and turbulent flux divergence with set D. As for Sodankylä, we found a positive turbulent heat flux divergence of ∼0.46–1.3 K h^{-1}, though this decreased to a negative value of $-0.64\,\mathrm{K\,h^{-1}}$ at 9 h. The radiative heat flux varied from −0.5 to $-0.93\,\mathrm{K\,h^{-1}}$ throughout the 9 h, again being of comparable size to the turbulent heat flux divergence.

We repeated the runs with the YSU–BL scheme in combination with set D forcings. Now, T_{2m} became up to 7 K too low. Temperatures aloft were simulated better with YSU than with MYJ, as illustrated by the strongly reduced biases (Table 5) and

Table 5. Mean bias error (MBE), root-mean-square error (RMSE) and median of the absolute error between model simulations and observations, for the period 8–17 h, for the Halley case for the following variables: 2 and 32 m temperature in K (T_{2m} and T_{32m}), 8 and 32 m wind speed in m s^{-1} ($U_{tot\,8m}$ and $U_{tot\,32m}$), 2 and 32 m specific humidity in g kg^{-1} (q_{2m} and q_{32m}), sensible (H) and soil heat flux (G) in W m^{-2}, net radiation in W m^{-2} (Q_{net}) and downward ($LW\downarrow$) and upward ($LW\uparrow$) long-wave radiation in W m^{-2}. Numbers in italic denote the run with the smallest bias between runs with various forcing methods (set A–D), those in bold the run with the lowest bias between all WRF–SCM runs (based on multiple decimals, D + q_{obs} is not included).

		A	B	C	D	D + q_{obs}	D + YSU	D + GFDL	D + CAM
MBE	T_{2m}	−5.5	−4.9	−4.8	*−1.4*	−0.9	−6.8	**−1.3**	−1.9
	T_{32m}	−9.5	−9.4	−9.3	*−4.8*	−4.6	**−1.0**	−4.7	−5.1
	$U_{tot\,8m}$	0.9	***−0.3***	−0.9	−0.9	−0.9	−1.1	−0.9	−0.9
	$U_{tot\,32m}$	3.8	1.8	*0.3*	0.4	0.4	**−0.1**	0.4	0.4
	q_{2m}	−0.14	−0.14	−0.14	*−0.11*	−0.03	**−0.04**	−0.11	−0.12
	q_{32m}	−0.27	−0.27	−0.27	*−0.23*	−0.08	**−0.19**	−0.23	−0.24
	H	−25.2	*−22.2*	−22.6	−26.8	−25.0	**−12.5**	−26.5	−27.7
	G	2.2	*1.8*	1.8	2.9	3.4	**0.8**	3.0	2.6
	Q_{net}	−32.8	*−30.4*	−30.7	−34.2	−32.9	**−22.5**	−33.9	−35.6
	$LW\downarrow$	−34.3	−34.1	−34.0	*−31.2*	−27.0	−31.8	**−30.2**	−34.5
	$LW\uparrow$	***−1.1***	−3.2	−2.9	3.5	6.4	−8.8	4.1	1.5
RMSE	T_{2m}	5.8	5.2	5.1	*2.2*	2.0	7.0	**2.2**	2.5
	T_{32m}	9.8	9.6	9.5	*4.9*	4.7	**1.7**	4.8	5.1
	$U_{tot\,8m}$	*1.0*	1.2	1.0	1.0	1.0	1.4	1.0	**1.0**
	$U_{tot\,32m}$	3.9	2.5	***0.5***	0.5	0.5	0.6	0.5	0.5
	q_{2m}	0.15	0.14	0.15	*0.12*	0.05	**0.08**	0.12	0.13
	q_{32m}	0.27	0.27	0.27	*0.24*	0.09	**0.20**	0.23	0.24
	H	25.5	23.3	*23.0*	27.0	25.2	**13.1**	26.8	27.9
	G	4.1	4.1	*3.9*	4.4	4.7	**3.4**	4.5	4.2
	Q_{net}	32.9	***30.8***	30.8	34.4	33.1	22.7	34.0	35.7
	$LW\downarrow$	34.3	34.1	34.1	*31.3*	27.2	31.9	**30.4**	34.6
	$LW\uparrow$	***1.8***	4.9	3.3	4.5	7.1	9.1	5.1	3.0
Median	T_{2m}	5.5	5.0	4.9	*1.5*	1.5	7.1	**1.4**	1.9
	T_{32m}	10.0	10.0	9.8	*4.9*	4.7	**1.1**	4.9	5.0
	$U_{tot\,8m}$	1.0	***0.9***	0.9	0.9	0.9	1.3	0.9	0.9
	$U_{tot\,32m}$	4.1	1.9	*0.4*	0.4	0.4	**0.3**	0.4	0.4
	q_{2m}	0.14	0.13	0.13	*0.10*	0.03	**0.05**	0.10	0.11
	q_{32m}	0.27	0.27	0.27	*0.23*	0.08	**0.17**	0.23	0.24
	H	25.2	24.3	*22.8*	27.9	26.1	**12.5**	27.9	29.0
	G	3.1	3.1	*3.0*	3.7	4.1	**2.3**	3.7	3.4
	Q_{net}	31.7	31.1	*30.1*	33.9	32.5	**22.6**	33.7	35.2
	$LW\downarrow$	34.0	33.6	33.8	*31.0*	26.9	31.6	**30.6**	34.4
	$LW\uparrow$	***1.7***	1.9	3.0	3.8	6.8	8.6	5.2	2.2

Note: Set E is omitted here, due to the non-physical behaviour below the threshold height for relaxation towards the 3D field.

the θ profile (Figure 9). Also, the temperature inversion improved substantially. A slightly larger bias was found for $U_{tot\,8m}$, where also stronger oscillations are simulated than for set D with MYJ, though a strong overestimated wind speed, as was found for Cabauw and Sodankylä, was not found for Halley. The wind-speed profile resembled the observations nicely, with a LLJ of the correct order of magnitude and only 10 m too high seen 9 h into the WRF–SCM simulation.

Large differences for q were found between MYJ and YSU. Right from the start, q_{2m} increased with YSU and followed the observed values nicely. The q profile was now totally different, with an almost well-mixed profile shape, which was not in agreement with the observed strong inversion. This higher amount of q was also seen with the Cabauw case.

Runs with set D were repeated with varying LW radiation schemes (D + GFDL and D + CAM). Differences between RRTMG and GFDL were very small, but with CAM a slightly lower T_{2m} (about 0.6 K) was found compared with RRTMG and $LW\downarrow$ was underestimated more (Table 5). The $LW\uparrow$ did improve when applying the CAM scheme, but overall $LW\uparrow$ biases were very small. As with the two cases studied previously, the choice of LW radiation scheme did not influence the wind-speed simulations.

6. Conclusion and discussion

Many numerical weather prediction and climate models experience difficulties in simulating stratified conditions, especially over snow and when low wind speeds are observed (e.g. Edwards *et al.*, 2011; Atlaskin and Vihma, 2012; Holtslag *et al.*, 2013). In this study, the WRF–3D and SCM, employed with the MYJ boundary-layer scheme, are evaluated for these conditions for three contrasting terrains with snow cover, these being Cabauw in the Netherlands (snow over grass/cropland), Sodankylä in Northern Finland (snow over a needle-leaf forest) and Halley in Antarctica (snow over an ice shelf). Though atmospheric conditions for all sites are not exactly equal, all cases are characterized by clear skies, stable stratification and near-surface wind speeds below 5 m s^{-1}.

For Cabauw and Sodankylä, WRF–3D experiments demonstrated that the default land-use settings gave incorrect output regarding the snow cover and vegetation fraction. This greatly influenced the soil heat flux and thus surface temperatures. Adjusting these settings with site-specific information improved the results.

Overall, the performance of 3D WRF was quite good, especially regarding the wind-speed simulations. Close to the surface, wind speeds were modelled correctly or with a very small overestimation for Cabauw and Sodankylä, while this was correct or slightly underestimated for Halley. Modelling the near-surface temperature appeared to be (more) challenging. T_{2m} was strongly overestimated up to 7 and 11 K for Cabauw and Sodankylä respectively at the end of the night, while the model performed better at higher tower levels. For Halley, T_{2m} was modelled more accurately during the SCM study period, while values were too low during the previous 8 h (5–10 K). Also, at higher levels temperatures remained too low for Halley. The three cases shared an underestimation of the modelled temperature gradient.

The WRF–3D fields were used to construct SCM forcings, where we distinguished between the following cases: A, not prescribing any lateral forcings; B, prescribing only time-varying geostrophic wind speed; C, prescribing momentum advection in addition to B; D, prescribing temperature and moisture advection in addition to C; and E, nudging the SCM to the 3D field at a height sufficiently above the BL. For all cases, we found that runs without lateral forcings and constant geostrophic wind speeds led to a substantial bias for wind speed. Prescribing momentum advection improved the modelled wind speed substantially, while model results for temperature, stratification and specific humidity improved considerably with set D. The nudging approach provided a deterioration of the model results and is therefore not advised. Hence, we conclude that prescribing time-varying geostrophic wind speed and momentum, temperature and humidity advection provides the best results for all sites.

Moreover, we conclude that model results are only marginally sensitive to the selected long-wave radiation schemes. Model simulations did show contrasting results between the MYJ and YSU boundary-layer schemes. YSU simulated a more stably stratified boundary layer than MYJ. For Sodankylä, the stratification became too strong, as reported by Sun and Barros (2013) and Kleczek *et al.* (2014) for other sites. With YSU, $T_{2\mathrm{m}}$ was better simulated for Cabauw and Sodankylä but strongly underestimated for Halley. Using YSU did degrade the simulated near-surface wind speed, which now remained too high, and simulated a LLJ at too low an altitude, consistent with the enhanced decoupling. The skill for q also decreased and values remained too high for Cabauw and Sodankylä. For Halley, q close to the surface improved but the profile became more mixed than found in observations.

Note that in this study we determined the advection at hour T_n as a residual term from the prognostic equations, for which the individual terms are based on WRF–3D results of the interval 1 h preceding (T_{n-1}) and 1 h following (T_{n+1}) hour T_n. Of course, one can also calculate the advection directly from the WRF–3D field (e.g. for temperature with $-\bar{U} \cdot \nabla\theta$). Then the advection is somewhat dependent on the order of the numerical spatial derivatives, while additionally the calculation of the advection close to the surface is hampered by varying terrain heights in the adjacent grid cells. Furthermore, this method provides more instantaneous fields, while the method applied here uses information for the previous and following hour and is in that respect more smooth.

Observations of the surface energy budget revealed a significant imbalance for all three sites. Surface energy balance closure is very challenging, especially over snow-covered surfaces and/or in stable conditions (Sánchez *et al.*, 2010; Chen *et al.*, 2011; Helgason and Pomeroy, 2012; Knowles *et al.*, 2012). Understanding the nature of this problem is beyond the scope of this article and constitutes a study area in itself (e.g. Heusinkveld *et al.*, 2004; Aubinet, 2008; Foken, 2008). However, it must be kept in mind when comparing the model results with the observed energy balance terms.

Possibly, improvements can be achieved in the representation of the snow pack. The Noah land-surface model has a bulk layer of snow and soil (Niu *et al.*, 2011), in which it adds the total snow depth as part of the first soil layer, making the resolution in snow rather poor (Figure 2). Particularly for Sodankylä, where the snow depth is 62 cm, this may have an effect. Moreover, when using the standard settings of WRF over sea ice, a constant snow conductivity in depth (though varying slightly in time with increasing density) is used, while a smooth transition from snow conductivity to ice conductivity would be more realistic when snow is gradually pressed to firn and ice.

It must also be mentioned that model results are grid-averaged, making a comparison against a local observation more difficult (Atlaskin and Vihma, 2012). According to Atlaskin and Vihma (2012), the comparison should therefore be made against observations that are averaged in that particular grid cell. However, such extensive measurements are uncommon for sites over snow.

All in all, the study shows that quite good results can be obtained for WRF–SCM runs for low wind speeds and three contrasting terrains for the cases studied, as long as proper advection of momentum, temperature and moisture is prescribed. This confirms the studies of Steeneveld *et al.* (2006) and Baas *et al.* (2010) and extends these findings for SBLs over snow. Additionally, we recommend a detailed prescription of the snow cover and vegetation fraction, since these variables influence the energy balance.

Although a perfect match between the model simulations and the observations has not been obtained, significant improvements were made with the right forcings. From this reference, the SCM can be used as a tool to study the small-scale processes in SBL modelling in order to improve our understanding of SBL processes. In Part 2 of this study, we will perform a sensitivity analysis with the WRF–SCM for the three cases of this particular study, where we focus on the processes of snow-surface coupling, radiation and turbulent mixing. In this way, we study their impact on the SBL evolution of the three cases and explore whether further agreement with observations can be achieved.

Acknowledgements

The authors are grateful to the Royal Netherlands Meteorological Institute (KNMI), the Finnish Meteorological Institute (FMI) and the British Antarctic Survey (BAS) for the measurement data that was used in this study. We thank ECMWF for the necessary boundary conditions for the WRF–3D runs that were obtained from their data server. We also thank Tiina Nygård for the discussions on the Halley data. We acknowledge support from The Dutch Science Foundation (NWO) with grant 829.09.005 ('Quantifying contributions of surface climate feedbacks to the Arctic amplification of greenhouse warming' in the Sustainable Earth program). The contribution by G. J. Steeneveld has been partly sponsored by the NWO contract 863.10.010 (Lifting the fog) and the work of T. Vihma was supported by the Academy of Finland (contracts 259537 and 263918). Finally, we thank the two anonymous reviewers for their valuable suggestions.

References

André JC, Mahrt L. 1982. The nocturnal surface inversion and influence of clear-air radiative cooling. *J. Atmos. Sci.* **39**: 864–878, doi: 10:1175=1520–0469(1982)039<0864:TNSIAI>2:0:CO; 2.

Atlaskin E, Vihma T. 2012. Evaluation of NWP results for wintertime nocturnal boundary-layer temperatures over Europe and Finland. *Q. J. R. Meteorol. Soc.* **138**: 1440–1451, doi: 10.1002/qj.1885.

Aubinet M. 2008. Eddy covariance CO2 flux measurements in nocturnal conditions: An analysis of the problem. *Ecol. Appl.* **18**: 1368–1378, doi: 10.1890/06-1336.1.

Baas P, Bosveld FC, Lenderink G, Van Meijgaard E, Holtslag AAM. 2010. How to design single-column model experiments for comparison with observed nocturnal low-level jets. *Q. J. R. Meteorol. Soc.* **136**: 671–684, doi: 10.1002/qj.592.

Batchvarova E, Gryning SE, Hasager CB. 2001. Regional fluxes of momentum and sensible heat over a sub-Arctic landscape during late winter. *Boundary-Layer Meteorol.* **99**: 489–507, doi: 10.1023/A:1018982711470.

Beljaars ACM, Bosveld FC. 1997. Cabauw data for the validation of land surface parameterization schemes. *J. Clim.* **10**: 1172–1193, doi: 10.1175/1520-0442(1997)010<1172:CDFTVO>2.0.CO;2.

Beljaars ACM, Holtslag AAM. 1991. Flux parameterization over land surfaces for atmospheric models. *J. Appl. Meteorol.* **30**: 327–341, doi: 10.1175/1520-0450(1991)030<0327:FPOLSF>2.0.CO;2.

Bosveld FC, Baas P, van Meijgaard E, de Bruijn EIF, Steeneveld GJ, Holtslag AAM. 2014a. The third GABLS intercomparison case for evaluation studies of boundary-layer models: Part A: Case selection and set-up. *Boundary-Layer Meteorol.* **152**: 133–156, doi: 10.1007/s10546-014-9917-3.

Bosveld FC, Baas P, Steeneveld GJ, Holtslag AAM, Angevine WM, Bazile E, de Bruijn EIF, Deacu D, Edwards JM, Ek M, Larson VE, Plein JE, Raschendorfer M, Svensson G. 2014b. The Third GABLS intercomparison case for evaluation studies of boundary-layer models: Part B: Results and process understanding. *Boundary-Layer Meteorol.* **152**: 157–187, doi: 10.1007/s10546-014-9919-1.

Brost RA, Wyngaard JC. 1978. A model study of the stably stratified planetary boundary layer. *J. Atmos. Sci.* **35**: 1427–1440, doi: 10.1175/1520-0469(1978)035<1427:AMSOTS>2.0.CO;2.

Byrkjedal Ø, Esau I, Kvamstø NG. 2008. Sensitivity of simulated wintertime Arctic atmosphere to vertical resolution in the ARPEGE/IFS model. *Clim. Dyn.* **30**: 687–701, doi: 10.1007/s00382-007-0316-z.

CESAR. 2013. Cabauw Experimental Site for Atmospheric Research. http://www.cesar-observatory.nl (accessed 13 February 2014).

Chen F, Dudhia J. 2001. Coupling an advanced land surface-hydrology model with the Penn State-NCAR MM5 modelling system. Part I: Model implementation and sensitivity. *Mon. Weather Rev.* **129**: 569–585, doi: 10.1175/1520-0493(2001)129<0569:CAALSH>2.0.CO;2.

Chen N, Guan D, Jin C, Wang A, Wu J, Yuan F. 2011. Influences of snow event on energy balance over temperate meadow in dormant season based on eddy covariance measurements. *J. Hydrol.* **399**: 100–107, doi: 10.1016/j.jhydrol.2010.12.037.

Chou MD, Suarez MJ. 1994. *An Efficient Thermal Infrared Radiation Parameterization for Use in General Circulation Models*, NASA Technical Memorandum 104606, vol. **3**. Goddard Space Flight Center: Greenbelt, MD. https://archive.org/stream/nasa_techdoc_19950009331/19950009331#page/n0/mode/2up (accessed 16 February 2014).

Delage Y. 1997. Parameterising sub-grid scale vertical transport in atmospheric models under statically stable conditions. *Boundary-Layer Meteorol.* **82**: 23–48, doi: 10.1023/A:1000132524077.

Edwards JM, McGregor JR, Bush MR, Bornemann FJ. 2011. Assessment of numerical weather forecasts against observations from Cardington: Seasonal diurnal cycles of screen-level and surface temperatures and surface fluxes. *Q. J. R. Meteorol. Soc.* **137**: 656–672, doi: 10.1002/qj.742.

Ek MB, Mitchell KE, Lin Y, Rogers E, Grunmann P, Koren V, Gayno G, Tarpley JD. 2003. Implementation of Noah land surface model advances in the National Centers for Environmental Prediction operational mesoscale Eta model. *J. Geophys. Res.* **108**: 8851, doi: 10.1029/2002JD003296.

ECMWF. 2013. *IFS Documentation Cy38r1, Operational Implementation 19 June 2012, Part IV: Physical Processes*. European Centre for Medium-Range Weather Forecasts (ECMWF): Reading, UK. http://old.ecmwf.int/research/ifsdocs/CY38r1/IFSPart4.pdf (accessed 31 January 2015).

FMI-ARC. 2013. Arctic Research Centre of the Finnish Meteorological Institute. http://fmiarc.fmi.fi (accessed 13 February 2014).

Foken T. 2008. The energy balance closure problem: An overview. *Ecol. Appl.* **18**: 1351–1367, doi: 10.1890/06-0922.1.

Garratt JR. 1992. *The Atmospheric Boundary Layer*. Cambridge University Press: Cambridge, UK.

Ghan SJ, Leung LR, McCaa J. 1999. A comparison of three different modeling strategies for evaluating cloud and radiation parameterizations. *Mon. Weather Rev.* **127**: 1967–1984, doi: 10.1175/1520-0493(1999)127<1967:ACOTDM>2.0.CO;2.

Gutman G, Ignatov A. 1998. The derivation of the green vegetation fraction from NOAA/AVHRR data for use in numerical weather prediction models. *Int. J. Remote Sens.* **19**: 1533–1543, doi: 10.1080/014311698215333.

Helgason W, Pomeroy J. 2012. Problems closing the energy balance over a homogeneous snow cover during midwinter. *J. Hydrometeorol.* **13**: 557–572, doi: 10.1175/JHM-D-11-0135.1.

Heusinkveld BG, Jacobs AFG, Holtslag AAM, Berkowicz SM. 2004. Surface energy balance closure in an arid region: role of soil heat flux. *Agric. For. Meteorol.* **122**: 21–37, doi: 10.1016/j.agrformet.2003.09.005.

Holland MM, Bitz CM. 2003. Polar amplification of climate change in coupled models. *Clim. Dyn.* **21**: 221–232, doi: 10.1007/s00382-003-0332-6.

Holton JR. 2004. *An Introduction to Dynamic Meteorology* (4th edn). Elsevier Academic Press: Burlington, MA.

Holtslag AAM, Boville BA. 1993. Local versus nonlocal boundary-layer diffusion in a global climate model. *J. Clim.* **6**: 1825–1842, doi: 10.1175/1520-0442(1993)006<1825:LVNBLD>2.0.CO;2.

Holtslag AAM, Steeneveld GJ, Van de Wiel BJH. 2007. Role of land-surface temperature feedback on model performance for the stable boundary layer. *Boundary-Layer Meteorol.* **125**: 361–376, doi: 10.1007/s10546-007-9214-5.

Holtslag AAM, Svensson G, Baas P, Basu S, Beare B, Beljaars ACM, Bosveld FC, Cuxart J, Lindvall J, Steeneveld GJ, Tjernström M, Van De Wiel BJH. 2013. Stable atmospheric boundary layers and diurnal cycles –challenges for weather and climate models. *Bull. Am. Meteorol. Soc.* **94**: 1691–1706, doi: 10.1175/BAMS-D-11-00187.1.

Hong SY. 2010. A new stable boundary-layer mixing scheme and its impact on the simulated East Asian summer monsoon. *Q. J. R. Meteorol. Soc.* **136**: 1481–1496, doi: 10.1002/qj.665.

Hong SY, Noh Y, Dudhia J. 2006. A new vertical diffusion package with an explicit treatment of entrainment processes. *Mon. Weather Rev.* **134**: 2318–2341, doi: 10.1175/MWR3199.1.

Hu X-M, Klein PM, Xue M. 2013. Evaluation of the updated YSU planetary boundary-layer scheme within WRF for wind resource and air quality assessments. *J. Geophys. Res. Atmos.* **118**: 10490–10505, doi: 10.1002/jgrd.50823.

Iacono MJ, Delamere JS, Mlawer EJ, Shephard MW, Clough SA, Collins WD. 2008. Radiative forcing by long-lived greenhouse gases: Calculations with the AER radiative transfer models. *J. Geophys. Res.* **113**: D13103, doi: 10.1029/2008JD009944.

Jiménez PA, Dudhia J, Fidel González-Rouco J, Navarro J, Montávez JP, García-Bustamante E. 2012. A revised scheme for the WRF surface layer formulation. *Mon. Weather Rev.* **140**: 898–918, doi: 10.1175/MWR-D-11-00056.1.

King JC Anderson PS. 1988. Installation and performance of the stable instrumentation at Halley. *Brit. Antarctic Surv. Bull.* **79**: 65–77.

King JC, Anderson PS. 1994. Heat and water vapour fluxes and scalar roughness lengths over an Antarctic ice shelf *Boundary-Layer Meteorol.* **69**: 101–121, doi: 10.1007/BF00713297.

Kleczek MA, Steeneveld GJ, Holtslag AAM. 2014. Evaluation of the Weather Research and Forecasting mesoscale model for GABLS3: Impact of boundary-layer schemes, boundary conditions and spin-up. *Boundary-Layer Meteorol.* **152**: 213–243, doi: 10.1007/s10546-014-9925-3.

KNMI. 2012. *Maandoverzicht van het Weer in Nederland*. Koninklijk Nederlands Meteorologisch Instituut, http://www.knmi.nl/klimatologie/mow/pdf/mow_201202.pdf (accessed 18 February 2014).

Knowles JF, Blanken PD, Williams MW, Chowanski KM. 2012. Energy and surface moisture seasonally limit evaporation and sublimation from snow-free alpine tundra. *Agric. For. Meteorol.* **157**: 106–115, doi: 10.1016/j.agrformet.2012.01.017.

Luce CH, Tarboton DG. 2001. A modified force-restore approach to modeling snow-surface heat fluxes. In *Proceedings of the 69th Annual Meeting of the western Snow Conference*, Sun Valley, ID, 17-19 April 2001, 103-114.

Mahrt L. 1999. Stratified atmospheric boundary layers. *Boundary-Layer Meteorol.* **90**: 375–396, doi: 10.1023/A:1001765727956.

Mahrt L, Sun J, Blumen W, Delany T, Oncley S. 1998. Nocturnal boundary-layer regimes. *Boundary-Layer Meteorol.* **88**: 255–278, doi: 10.1023/A:1001171313493.

Mellor GL, Yamada T. 1982. Development of a turbulence closure model for geophysical fluid problems. *Rev. Geophys. Space Phys.* **20**: 851–875, doi: 10.1029/RG020i004p00851.

NCAR UCAR. 2013. 'Current AMPS configuration'. http://www2.mmm.ucar.edu/rt/amps/information/configuration/configuration.html (accessed 31 January 2015).

Niu GY, Yang ZL, Mitchell KE, Chen F, Ek MB, Barlage M, Kumar A, Manning K, Niyogi D, Rosero E, Tewari M, Xia Y. 2011. The community Noah land surface model with multiparameterization options (Noah-MP): 1. Model description and evaluation with local-scale measurements. *J. Geophys. Res.* **116**: D12109, doi: 10.1029/2010JD015139.

Oldroyd HJ, Higgins CW, Huwald H, Selker JS, Parlange MB. 2013. Thermal diffusivity of seasonal snow determined from temperature profiles. *Adv. Water Resour.* **55**: 121–130, doi: 10.1016/j.advwatres.2012.06.011.

Rinke A, Dethloff K, Cassano JJ, Christensen JH, Curry JA, Du P, Girard E, Haugen J-E, Jacob D, Jones CG, Køltzow M, Laprise R, Lynch AH, Pfeifer S, Serreze MC, Shaw MJ, Tjernström M, Wyser K, Žagar M. 2006. Evaluation of an ensemble of Arctic regional climate models: Spatiotemporal fields during the SHEBA year. *Clim. Dyn.* **26**: 459–472, doi: 10.1007/s00382-005-0095-3.

Rinke A, Ma Y, Bian L, Xin Y, Dethloff K, Persson POG, Lüpkes C, Xiao C. 2012. Evaluation of atmospheric boundary-layer surface process relationships in a regional climate model along an East Antarctic traverse. *J. Geophys. Res.* **117**: D09121, doi: 10.1029/2011JD016441.

Rostkier-Edelstein D, Hacker JP. 2010. The roles of surface-observation ensemble assimilation and model complexity for nowcasting of PBL profiles: A factor separation analysis. *Weather and Forecasting* **25**: 1670–1690, doi: 10.1175/2010WAF2222435.1.

Sánchez JM, Caselles V, Rubio EM. 2010. Analysis of the energy balance closure over a FLUXNET boreal forest in Finland. *Hydrol. Earth Syst. Sci.* **14**: 1487–1497, doi: 10.5194/hess-14-1487-2010.

Savijärvi H. 2006. Radiative and turbulent heating rates in the clear-air boundary layer. *Q. J. R. Meteorol. Soc.* **132**: 147–161, doi: 10.1256/qj.05.61.

Savijärvi H. 2013. High-resolution simulations of the night-time stable boundary layer over snow. *Q. J. R. Meteorol. Soc.* **140**: 1121–1128, doi: 10.1002/qj.2187.

Skamarock WC, Klemp JB, Dudhia J, Gill DO, Barker DM, Duda MG, Huang XY, Wang W, Powers JG. 2008. *A Description of the Advanced Research WRF Version 3*. Mesoscale and Microscale Meteorology Division, National Center for Atmospheric Research (NCAR): Boulder, CO. http://www2.mmm.ucar.edu/wrf/users/docs/arw_v3.pdf (accessed 31 January 2015).

Steeneveld GJ, Van de Wiel BJH, Holtslag AAM. 2006. Modeling the evolution of the atmospheric boundary layer coupled to the land surface for three contrasting nights in CASES-99. *J. Atmos. Sci.* **63**: 920–935, doi: 10.1175/JAS3654.1.

Sterk HAM, Steeneveld GJ, Holtslag AAM. 2013. The role of snow-surface coupling, radiation, and turbulent mixing in modeling a stable boundary layer over Arctic sea ice. *J. Geophys. Res. Atmos.* **118**: 1199–1217, doi: 10.1002/jgrd.50158.

Stull RB. 1988. *An Introduction to Boundary-Layer Meteorology*. Kluwer Academic Publishers: Dordrecht, Netherlands.

Sturm M, Perovich DK, Holmgren J. 2002. Thermal conductivity and heat transfer through the snow on the ice of the Beaufort Sea. *J. Geophys. Res.* **107**: SHE 19-1–SHE 19-17, doi: 10.1029/2000JC000409.

Sun X, Barros AP. 2013. High resolution simulation of tropical storm *Ivan* (2004) in the Southern Appalachians: Role of planetary boundary-layer schemes and cumulus parametrization. *Q. J. R. Meteorol. Soc.* **140**: 1847–1865, doi: 10.1002/qj.2255.

Svensson G, Holtslag AAM. 2009. Analysis of model results for the turning of the wind and related momentum fluxes in the stable boundary layer. *Boundary-Layer Meteorol.* **132**: 261–277, doi: 10.1007/s10546-009-9395-1.

Svensson G, Karlsson J. 2011. On the Arctic wintertime climate in Global Climate Models. *J. Clim.* **24**: 5757–5771, doi: 10.1175/2011JCLI4012.1.

Tardif R. 2007. The Impact of Vertical Resolution in the Explicit Numerical Forecasting of Radiation Fog: A Case Study. *Pure Appl. Geophys.* **164**: 1221–1240, doi: 10.1007/s00024-007-0216-5.

Tastula EM, Vihma T. 2011. WRF model experiments on the Antarctic atmosphere in winter. *Mon. Weather Rev.* **139**: 1279–1291, doi: 10.1175/2010MWR3478.1.

Tjemkes SA, Duynkerke PG. 1989. The nocturnal boundary layer: Model calculations compared with observations. *J. Appl. Meteorol.* **28**: 161–175, doi: 10.1175/1520-0450(1989)028<0161:TNBLMC>2.0.CO;2.

Troen IB, Mahrt L. 1986. A simple model of the atmospheric boundary layer; sensitivity to surface evaporation. *Boundary-Layer Meteorol.* **37**: 129–148, doi: 10.1007/BF00122760.

Van Ulden AP, Holtslag AAM. 1985. Estimation of atmospheric boundary layer parameters for diffusion applications. *J. Climate Appl. Meteorol.* **24**: 1196–1207, doi: 10.1175/1520-0450(1985)024<1196:EOABLP>2.0.CO;2.

Van Ulden AP, Wieringa J. 1996. Atmospheric boundary layer research at Cabauw. *Boundary-Layer Meteorol.* **78**: 39–69, doi: 10.1007/BF00122486.

Valkonen T, Vihma T, Johansson MM, Launiainen J. 2013. Atmosphere–sea ice interaction in early summer in the Antarctic: Evaluation and challenges of a regional atmospheric model. *Q. J. R. Meteorol. Soc.* **140**: 1536–1551, doi: 10.1002/qj.2237.

Van de Wiel BJH, Moene AF, Jonker HJJ, Baas P, Basu S, Donda JMM, Sun J, Holtslag AAM. 2012. The minimum wind speed for sustainable turbulence in the nocturnal boundary layer. *J. Atmos. Sci.* **69**: 3116–3127, doi: 10.1175/JAS-D-12-0107.1.

Vihma T, Johansson MM, Launiainen J. 2009. Radiative and turbulent surface heat fluxes over sea ice in the western Weddell Sea in early summer. *J. Geophys. Res.* **114**: C04019, doi: 10.1029/2008JC004995.

Vogelezang DHP, Holtslag AAM. 1996. Evaluation and model impacts of alternative boundary-layer height formulations. *Boundary-Layer Meteorol.* **81**: 245–269, doi: 10.1007/BF02430331.

Walsh JE, Chapman WL, Romanovsky V, Christensen JH, Stendel M. 2008. Global climate model performance over Alaska and Greenland. *J. Clim.* **21**: 6156–6174, doi: 10.1175/2008JCLI2163.1.

Wang Z, Zeng X. 2009. Using satellite and in situ data to evaluate snow albedo schemes in weather and climate models. *Extended Abstract, 16th Conference on Satellite Meteorology and Oceanography*. American Meteorological Society: Phoenix, AZ https://ams.confex.com/ams/pdfpapers/143743.pdf (accessed 16 February 2014).

Wetzel PJ. 1982. Toward parameterization of the stable boundary layer. *J. Appl. Meteorol.* **21**: 7–13, doi: 10.1175/1520-0450(1982)021<0007:TPOTSB>2.0.CO;2.

Williams AG, Chambers S, Griffiths A. 2013. Bulk mixing and decoupling of the nocturnal stable boundary layer characterized using a ubiquitous natural tracer. *Boundary-Layer Meteorol.* **149**: 381–402, doi: 10.1007/s10546-013-9849-3.

Zhang T, Stamnes K, Bowling SA. 2001. Impact of the atmospheric thickness on the atmospheric downwelling longwave radiation and snowmelt under clear-sky conditions in the Arctic and Subarctic. *J. Clim.* **14**: 920–939, doi: 10.1175/1520-0442(2001)014<0920:IOTATO>2.0.CO;2.

